

Florent Lyard · Fabien Lefevre · Thierry Letellier ·
Olivier Francis

Modelling the global ocean tides: modern insights from FES2004

Received: 25 February 2006 / Accepted: 9 June 2006 / Published online: 27 September 2006
© Springer-Verlag 2006

Abstract During the 1990s, a large number of new tidal atlases were developed, primarily to provide accurate tidal corrections for satellite altimetry applications. During this decade, the French tidal group (FTG), led by C. Le Provost, produced a series of finite element solutions (FES) tidal atlases, among which FES2004 is the latest release, computed from the tidal hydrodynamic equations and data assimilation. The aim of this paper is to review the state of the art of tidal modelling and the progress achieved during this past decade. The first sections summarise the general FTG approach to modelling the global tides. In the following sections, we introduce the FES2004 tidal atlas and validate the model against in situ and satellite data. We demonstrate the higher accuracy of the FES2004 release compared to earlier FES tidal atlases, and we recommend its use in tidal applications. The final section focuses on the new dissipation term added to the equations, which aims to account for the conversion of barotropic energy into internal tidal energy. There is a huge improvement in the hydrodynamic tidal solution and energy budget obtained when this term is taken into account.

Keywords Tidal atlas · Finite element modelling · FES2004 · Data assimilation

Responsible editor: Bernard Barnier

F. Lyard (✉) · T. Letellier
Laboratoire LEGOS, UMR 5566, Observatoire Midi-Pyrénées,
Toulouse, France
e-mail: Florent.Lyard@cnes.fr

F. Lefevre
CLS,
Ramonville St. Agnes,
Toulouse, France

O. Francis
Université du Luxembourg, ECGS,
Walferdange, Luxembourg, Belgium

1 Introduction

The description, understanding, and quantitative determination of the ocean tides has attracted a long series of brilliant mathematicians and physicians in the history of science. In the early eighties, computer technology allowed us, for the first time, to generate global, realistic tidal models, notably the Naval Surface Weapon Center (NSWC) model, which was based on the solution of the hydrodynamic equation of the tides constrained with tidal gauge observation (Schwiderski 1980). Although it had unprecedented accuracy, the NSWC model was not accurate enough for the forthcoming satellite altimetry missions, which depended on precise tidal estimates for orbit determination and for ocean sea level de-aliasing. Within the framework of the Topex/Poseidon (T/P) mission, the international tidal community has undertaken a huge effort to improve or develop new tidal models, with the objective of attaining a centimetre accuracy level in tidal prediction, necessary to meet the altimetry product requirements (Le Provost et al. 1995). This international effort quickly split into two main approaches: the so-called empirical approach based on the direct analysis of the altimetry sea level time series (initiated by Cartwright and Ray 1991), and a modelling approach based on hydrodynamic and assimilation models. Later on, the interaction between the two approaches (i.e. data assimilation based on altimetry analysis on one hand, and hydrodynamic/assimilation modelling on the other hand) was a key factor for the overall success in improving tidal prediction accuracy and reaching the T/P requirements.

Within the tidal community, the Grenoble group *Modélisation des Ecoulements Océaniques à Moyenne et grande échelle*, led by C. Le Provost, followed the second approach by developing the hydrodynamic model *Code aux Eléments Finis pour la Marée Océanique* (CEFMO) and the associated assimilation model *Code d'Assimilation de Données Orienté Représenteur* (CADOR). The tidal atlases produced from those models received the generic name of finite element solutions (FES). The major releases formed a nearly continuous bi-annual production between

1992 and 2004, including the FES95 (Le Provost et al. 1998), FES99 (Lefevre et al. 2002) and FES2004 tidal atlases. The spectral and finite element characteristics of the CEFMO model proved to be key factors for the success of the FES atlases. The relatively cheap computational cost of the spectral system allowed us to optimise the number of finite elements in the ocean discretisation, hence improving the tidal energy dissipation in shelf regions and local tidal conditions with unchallenged precision for a global ocean model. In addition, the early introduction of loading and self-attraction (LSA) terms in the tidal equation allowed us to compute highly accurate hydrodynamic solutions for basin scale applications, especially in the Atlantic Ocean. In parallel, the CADOR assimilation code was developed from the original Bennett and McIntosh (1982) representer formulation (see also Egbert et al. 1994). Due to computer limitations, the global tides are obtained from basin solutions obtained from a Schur (or block resolution)-like method developed in 1997. Because of the quasi-linearity of the CEFMO equations (see Section 2.1), this approach is highly efficient and is equivalent to the resolution of the true global problem. The first published tidal atlas produced by using these techniques was the FES99 atlas. Continuous improvements in the model and data have motivated the production of further atlases, of which the most recent release is the FES2004 atlas.

The aim of this paper is to provide a global overview of the modelling and data assimilation approach as well as the recent FES solutions. Because the FES2004 atlas is likely to be the last tidal atlas produced from the CEFMO and CADOR models, the authors wish to highlight some technical issues that were not addressed in previous publications. Sections 2 and 3 will briefly introduce the tidal equations for the hydrodynamic and assimilation codes. The FES2004 atlas and its validation are developed in Section 4. Details of the atlas production are given and some particular aspects of the tidal spectrum components are also discussed. Section 5 is devoted to tidal energy dissipation, introducing the newly added parameterisation of barotropic to baroclinic energy conversion. This last point is one of the major breakthroughs of the altimetry observation mission (Egbert and Ray 2000), not only for the tidal modelling itself but also because of its implications for the general ocean circulation. This paper is dedicated to Christian Le Provost, who passed away in 2004. His leadership and vision in tidal science has broadly contributed to the great success of modelling ocean tides during the past decades and, consequently, of the satellite ocean altimetry mission.

2 CEFMO tidal equations

2.1 Fundamental hydrodynamic equations

The purpose of this section is to briefly introduce the differential equations used in the hydrodynamic solvers

and data assimilation software. The detailed developments can be found in previous publications (Le Provost et al. 1981; Le Provost and Vincent 1986). The CEFMO tidal equations are derived from the classical shallow water equations where the advection and horizontal viscosity term is neglected. Assuming the existence of a dominant tidal constituent (in terms of currents), the friction terms are obtained in a tensor form as a linear development of the non-linear bottom drag given by:

$$\boldsymbol{\tau} = \frac{C}{H} \|\mathbf{u}\| \mathbf{u} \quad (1)$$

where \mathbf{u} is the depth-averaged tidal velocity, H the mean local depth and C a dimensionless friction coefficient usually taken as 2.5×10^{-3} . Once the problem is fully linearised, we can solve complex equations in the spectral domain. The quasi-linearised, complex tidal equations can then be written for any astronomical tidal constituent as:

$$j\omega\alpha + \nabla \cdot H\mathbf{u} = 0 \quad (2)$$

$$j\omega\mathbf{u} + \mathbf{f} \times \mathbf{u} = -g\nabla \cdot (\alpha + \delta) + g\nabla\Pi - \mathbf{D}\mathbf{u} \quad (3)$$

where $j = \sqrt{-1}$, ω is the tidal frequency in rad/s, δ the ocean bottom radial displacement, α the ocean tide elevation, Π the total tidal potential (i.e. astronomical plus loading/self-attraction potential), \mathbf{D} the drag tensor, $\mathbf{f} = 2\Omega\mathbf{k}$ the Earth rotation vector and g the gravity constant. The boundary conditions are the classical zero-flux Neuman conditions on tidal currents along the rigid (or closed) boundaries $\partial\Omega_o$, and clamped (or Dirichlet) conditions on tidal elevations at the open ocean boundaries $\partial\Omega_o$.

In the early version of CEFMO, the complex tensor $\mathbf{D} = \begin{bmatrix} r & r' \\ r'' & r''' \end{bmatrix}$ is limited to the bottom drag contribution, and its coefficients depend only on the dominant wave currents (as discussed in Section 5, additional terms have been added later to account for the wave drag energy dissipation). The bottom friction tensor is identical for all tidal components, except the dominant wave itself. Because the tidal velocities for the dominant component are not known before the tidal equations are resolved, we use an iterative method initialised with approximate currents (about 1 m/s). Quasi-convergence is reached after a limited number of iterations, typically less than 10 (i.e. convergence of the currents nearly occurs everywhere except in some very non-linear, shallow water regions). Once the dominant constituent is resolved, the rest of the tidal spectrum can be solved in a one-step manner. In practice, we extend the method to a dominant wave couple, namely, M_2 and K_1 , which is solved in an embedded iterative scheme, to account for the few local regions where the diurnal tidal currents are larger than the semi-diurnal ones.

The ocean bottom radial displacement $\delta(\lambda, \phi)$ due to the solid Earth tides and loading effects is:

$$\delta(\lambda, \varphi) = h_2 \Pi_a(\lambda, \varphi) + \int G_\delta(\lambda, \varphi, \lambda', \varphi') \alpha(\lambda, \varphi) ds \quad (4)$$

where h_2 is the deformation Love number, $\Pi_a(\lambda, \phi)$ the astronomical potential expressed in metres (i.e. divided by the gravity constant g), and G_δ the elastic Green's functions. The total tidal potential is the sum of the astronomical tidal potential plus the tidal self-attraction and gravity perturbation potential due to the ocean bottom displacement:

$$\Pi(\lambda, \varphi) = (1 + k_2) \Pi_a(\lambda, \varphi) + \int G_\pi(\lambda, \varphi, \lambda', \varphi') \alpha(\lambda, \varphi) ds \quad (5)$$

Here, $\int G_\delta(\lambda, \varphi, \lambda', \varphi') \alpha(\lambda, \varphi) ds$ and $\int G_\pi(\lambda, \varphi, \lambda', \varphi') \alpha(\lambda, \varphi) ds$ are the convolution integrals between a pre-existing tidal solution and the appropriate Green's functions (see Farrell 1972; Francis and Mazzega 1990). In practice, the convolution terms in Eqs. 4 and 5 are put together in a so-called LSA term. In theory, this linear term could be integrated implicitly into the tidal equations. However, this would make the tidal dynamic system matrix dense instead of band, because of the systematic node-to-node connections coming from the global ocean convolution, and thus making the matrix practically impossible to invert even with heavy computational means. The explicit method (i.e. LSA computed from a pre-existing tidal solution) is much more efficient, but at a price! Firstly, the new tidal solution may be inconsistent with the LSA prescribed in the forcing terms, which can induce an erroneous non-zero global rate of work of the LSA forcing. Secondly, this approach is less accurate in shelf and coastal regions, because here the tides and LSA show very rapid spatial variability, which can be captured differently by the tidal model and the pre-existing solution used to compute the LSA terms. Using a standard iteration scheme to successively solve the tides, and then estimate new LSA forcing from the so-obtained solution, and so forth, is known to be poorly convergent and inefficient. However, this technique is more successful when iterating not on the LSA itself but on the departure of LSA from its linear approximation [such as suggested by Accad and Pekeris (1978), and carried out by Egbert et al. (2004)]. This linear approximation (i.e. LSA being taken as about 10% of the local tidal elevation) can be easily taken as implicit in the tidal system without damaging the matrix bandwidth, and the convergence on the LSA is proved to be rapid.

A similar form of the equations can be derived for the non-linear constituents, where the tidal potential forcing

terms are set equal to zero and are replaced by the non-linear terms that apply to astronomical waves. For instance, the M_4 constituent linearised equations are given by:

$$j\omega\alpha + \nabla \cdot H\mathbf{u} = -\nabla \cdot \varphi_c(\eta_{M_2}, \mathbf{u}_{M_2}) \quad (6)$$

$$j\omega\mathbf{u} + \mathbf{f} \times \mathbf{u} = -g\nabla(\alpha - \delta) - D\mathbf{u} - \varphi_m(\mathbf{u}_{M_2}, \nabla\mathbf{u}_{M_2}) \quad (7)$$

where $\varphi_c(\eta_{M_2}, \mathbf{u}_{M_2})$ and $\varphi_m(\mathbf{u}_{M_2}, \nabla\mathbf{u}_{M_2})$ are the non-linear forcing functions expressing the complex contributions of the M_2 constituent at the M_4 frequency in the continuity and the momentum equations, respectively. These functions show significant value only where \mathbf{u}_{M_2} , $\nabla\mathbf{u}_{M_2}$ and η_{M_2} are substantial, namely in the shallow seas. In practice, the computation of non-linear constituents from the spectral model is a tedious task with only limited benefits for deep-ocean-tide prediction (which was the primary objective of the FES series of atlases). Therefore, the non-linear tides were not included in the early FES atlases. With the growing focus on shelf and coastal regions, the non-linear constituents can no longer be ignored. For the FES2004 model, the MOG2D time-stepping, non-linear, shallow-water, finite-element P1 model (Carrère and Lyard 2003) was used to compute the non-linear constituents on the FES2004 grid, and the M_4 constituent has now been added to the FES2004 atlas (see section below).

2.2 Discretised equations

The linearised momentum Eq. 3 can be expressed in a matrix form as:

$$H\mathbf{u} = \mathbf{M}(\nabla\alpha - \mathbf{F}) \quad (8)$$

$$\text{where } \mathbf{M} = -\frac{gH}{\Delta} \begin{bmatrix} i\omega + r''' & f - r' \\ -f - r'' & i\omega + r \end{bmatrix} \quad \text{and} \\ \Delta = \det \begin{pmatrix} i\omega + r & r' - f \\ r'' + f & i\omega + r''' \end{pmatrix}$$

Substituting Eq. 8 in Eq. 2 yields the spectral wave equation:

$$S[\alpha](\mathbf{x}) = \frac{1}{\kappa} (i\omega\alpha + \nabla \cdot \mathbf{M}\nabla\alpha)(\mathbf{x}) = \Psi(\mathbf{x}) \\ = \frac{1}{\kappa} (F_\alpha + \nabla \cdot \mathbf{M}\mathbf{F})(\mathbf{x}) \quad (9)$$

where κ is a numerical normalisation factor and F_α is zero for astronomical tides. The tidal equations are discretised over a triangular mesh and solved under the weak

formulation. For any computational node n in the domain (except the open-boundaries nodes, where clamped conditions in elevation are applied), the weak formulation of the wave equation takes the form:

$$\langle S[\alpha], \beta_n \rangle = \int_{\Omega} S[\alpha](\mathbf{x})\beta_n(\mathbf{x})ds = \int_{\Omega} \Psi(\mathbf{x})\beta_n(\mathbf{x})ds \quad (10)$$

where β_n is the P2-Lagrange interpolation associated with node n (piecewise second-order interpolation). Green's formula is used to transform the wave equation in the following manner:

$$\begin{aligned} \int_{\Omega} (\nabla \cdot H\mathbf{u})\beta_n ds &= \int_{\Omega} (\nabla \cdot \beta_n H\mathbf{u} - H\mathbf{u} \cdot \nabla \beta_n) ds \\ &= \oint_{\Gamma} \beta_n H\mathbf{u} \cdot \mathbf{n} dl - \int_{\Omega} H\mathbf{u} \cdot \nabla \beta_n ds \end{aligned} \quad (11)$$

Finally, the discrete wave equation is solved in the following form:

$$\begin{aligned} \langle S[\alpha], \beta_n \rangle &= \int_{\Omega} (i\omega\alpha + \nabla\beta_n \cdot \mathbf{M}\nabla\alpha)(\mathbf{x})ds \\ &= \int_{\Omega} \nabla\beta_n \cdot \mathbf{M}\mathbf{F}(\mathbf{x})ds \end{aligned} \quad (12)$$

The boundary integral vanishes under the rigid (zero-flux) boundary conditions. Once the tidal elevation system is solved, the tidal currents can be deduced from Eq. 8. Note that explicit computations with Eq. 8 are ill-defined at finite element edges and vertices (cross-edge discontinuities coming from triangle dependant derivation), and therefore a weak formulation approach is, in principle, needed to solve for the tidal currents.

2.3 Model finite element mesh

The two main advantages of using a finite-element discretisation are to better follow the coastline geometry and to optimise the trade-off between computational cost and model accuracy. Away from the coastal boundaries, the resolution is constrained by the classical wavelength criterion set on the finite element sides elements (Le Provost and Vincent 1986; Greenberg et al. 2006):

$$\lambda_{\eta} = \frac{T}{15} \sqrt{gH} \quad (13)$$

where λ_{η} is the element's side length, T the tidal wave period, g the gravity constant and H the local depth. The minimum number of Lagrange-P2 computational points over a tidal wavelength was set to 30, corresponding to 15 finite elements. As semi-diurnal tides demand a higher resolution compared to the diurnal and long-period tides, T is taken to be the period of the M_2 tide. This criterion will increase the model resolution in the shallower areas, such as the continental shelves. The FES94, FES95 and FES99 atlases have been computed on the Global Finite Element Model-1 (GFEM-1) triangular finite element mesh designed originally for early basin-wide studies at the beginning of the T/P project. Its resolution is about 20 km along the coastlines (i.e. corresponding to a 10-km resolution in Lagrange-P2 discretisation), with maximum-elements side reaching 400 km in the deepest part of the global ocean (i.e. corresponding to a 200-km numerical resolution). The total number of computational nodes in GFEM-1 is about 340,000. However, due to its piecewise construction, the GFEM-1 mesh was rather inhomogeneous in terms of spatial resolution. It also did not include some marginal seas, such as the Persian Gulf, the Red Sea and the Gulf of Maine, which were discarded to save some computational CPU time. A decision was made to refurbish the global mesh for the tidal atlases beginning with FES99 (Lefevre 2004). The GFEM-2 finite-element mesh was re-designed to homogenise, improve and extend the finite element mesh and provide more complete ocean coverage, including some missing marginal seas, such as the Black Sea, the Baltic Sea and the Bay of Fundy. In addition, a new geometric constraint was added to improve tidal current solutions over steep topographic slopes:

$$\lambda_u = \frac{2\pi}{15} \frac{H}{|\nabla H|} \quad (14)$$

where λ_u is the element's side length, H the local depth and $|\nabla H|$ the modulus of the local slope. This criterion will increase the model resolution at the shelf break and over steep volcanic ridges. This criterion is much more demanding than the wavelength criterion, and it has been only partially applied to constrain the new mesh. The new GFEM-2 mesh, shown in Fig. 1, contains about 500,000 elements and 1,000,000 computational nodes.

3 CADOR assimilation method

The CADOR assimilation software is based on the representer approach (Bennett and McIntosh 1982; Bennett 1990; Egbert et al. 1994). The full development of the assimilation code is described by Lyard (1999), and here we present the key points for assimilating pointwise, harmonic sea elevation data. We define the linear observation operator, which corresponds to available sea-

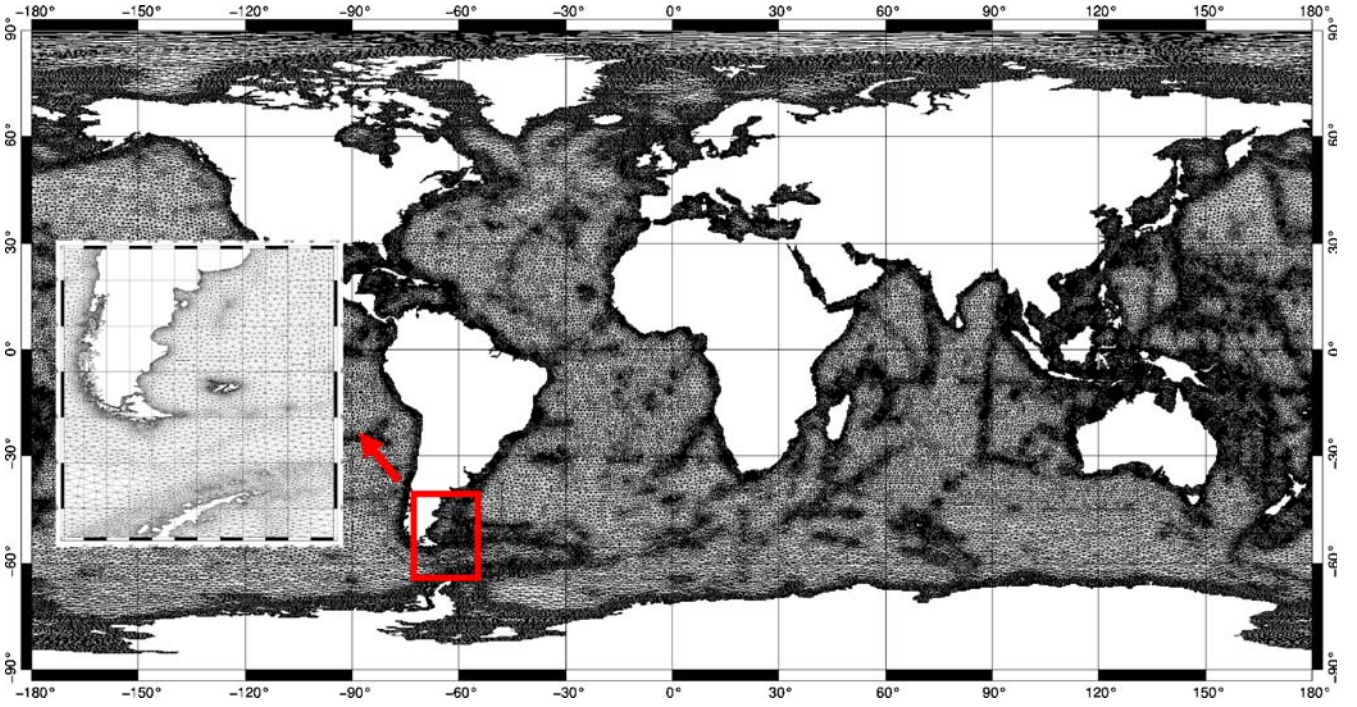


Fig. 1 GFEM-2 finite element mesh (FES2002/2004 tidal atlas)

surface harmonic data d_k , located strictly inside the modelling domain under the integral form:

$$L_k(\alpha) = \int_{\Omega} \mu_k^*(\mathbf{x})\alpha(\mathbf{x})ds \quad (15)$$

where α is the ocean tide complex elevation and μ_k is equivalent to the kernel of the observation operator. In the case of pointwise observations, μ_k is the Dirac function associated with the k th data spatial location \mathbf{x}_k . Considering the whole set of assimilated data, the model misfit vector can be expressed as $\mathbf{e} = \mathbf{d} - \mathbf{L}[\alpha] = [d_k - L_k[\alpha]]$. The assimilation problem is based on L2 norm (quadratic) cost function, defined as follows:

$$\begin{aligned} J(\alpha) = & \mathbf{e}^* \mathbf{C}_\varepsilon^{-1} \mathbf{e} + \int_{\Omega} \partial\psi^*(\mathbf{x})C_i^{-1}[\partial\psi](\mathbf{x})ds \\ & + \int_{\partial\Omega_o} \partial\alpha_o^*(\mathbf{x})C_o^{-1}[\partial\alpha_o](\mathbf{x})dl \\ & + \int_{\partial\Omega_c} \partial\Phi^*(\mathbf{x})C_i^{-1}[\delta\Phi](\mathbf{x})dl \end{aligned} \quad (16)$$

where C_ε is the error covariance matrix for observations, C_i , C_o and C_c the error covariance operators associated with interior forcing errors, open boundary conditions errors and rigid boundary conditions errors, respectively.

The first term quantifies the misfit between the α solution and data and the last three terms quantify the misfits between α and the prior solution taken as a function of the internal forcing and boundary conditions. The assimilation solution is the α field that minimises the above cost function.

3.1 Representer approach

The minimisation of the cost function can be done by different techniques. In CADOR, we follow the representer approach which has the great advantage of being dimensioned by the number of assimilated data K . Ignoring non-trivial mathematic details and assuming that the linear operators C_i , C_o and C_c have an inverse, we define the C-scalar product as follows:

$$\begin{aligned} \langle \alpha_1, \alpha_2 \rangle_C = & \int_{\Omega} (S[\alpha_1])^* C_i^{-1} [S[\alpha_2]] ds \\ & + \int_{\partial\Omega_o} \alpha_1^* C_o^{-1} [\alpha_2] dl \\ & + \int_{\partial\Omega_c} (\mathbf{M}\nabla\alpha_1 \cdot \mathbf{n})^* C_c^{-1} [\mathbf{M}\nabla\alpha_2 \cdot \mathbf{n}] dl \end{aligned} \quad (17)$$

for each assimilated datum, the k th observation linear form can be associated with a representer field r_k defined over

the domain so that the observation of the α field is equal to its C-scalar product with r_k :

$$\begin{aligned} L_k(\alpha) = \langle r_k, \alpha \rangle_C &= \int_{\Omega} (S[r])^* C_i^{-1} [S[\alpha]] ds \\ &+ \int_{\partial\Omega_o} r^* C_o^{-1} [\alpha] dl \\ &+ \int_{\partial\Omega_c} (\mathbf{M}\nabla r \cdot \mathbf{n})^* C_c^{-1} [\mathbf{M}\nabla\alpha \cdot \mathbf{n}] dl \end{aligned} \quad (18)$$

Then, the assimilation solution is sought as the sum of the prior solution plus a linear combination of the data representers, i.e.:

$$\alpha(\mathbf{x}) = \alpha_{\text{prior}}(\mathbf{x}) + \sum_{k=1}^K b_k r_k(\mathbf{x}) \quad (19)$$

At this point, we have reduced the minimisation problem from an infinite dimension to a finite dimension, with K degrees of freedom for the b_k coefficients. The original cost function simplifies into two terms, the first one being unchanged and the last three concentrated into a unique term accounting for the entire misfits with the prior solution:

$$J(\alpha) = (\mathbf{d} - \mathbf{L}[\alpha])^* \mathbf{C}_\varepsilon^{-1} (\mathbf{d} - \mathbf{L}[\alpha]) + \mathbf{b}^* \mathbf{R} \mathbf{b} \quad (20)$$

where $R_{ij} = \langle r_i, r_j \rangle_C = L_i[r_j] = \langle r_i, r_j \rangle_C^* = L_j^*[r_i]$. \mathbf{R} is the Hermitian representer matrix. The b_k coefficients that minimise Eq. 20 are solutions of the $K \times K$ system:

$$(\mathbf{R} + \mathbf{C}_\varepsilon) \mathbf{b} = \mathbf{e}_{\text{prior}} \quad (21)$$

Therefore, the data assimilation solution burden consists mainly in computing the representers associated with the data.

3.2 Representer equations

It can be shown that the representer is the solution of a two-step system. To simplify the following equations, we set $\mathbf{M}\nabla\alpha = \alpha$, $\mathbf{M}\nabla r = r$ and $\mathbf{M}^*\nabla\eta = \eta$, and we drop the data index. The first step involves developing a so-called backwards, or adjoint, model of the hydrodynamic wave equation model:

$$S^\diamond[\eta] = \frac{1}{\kappa} (-i\omega\eta + \nabla \cdot \mathbf{M}^*\nabla\eta) = \mu \quad (22)$$

with open boundary conditions

$$\eta(x) = 0 \quad \forall x \in \partial\Omega_o \quad (23)$$

and rigid boundary conditions

$$\eta \cdot \mathbf{n} = 0 \text{ on } \partial\Omega_c \quad (24)$$

where \mathbf{M}^* is the canonical adjoint matrix of the matrix operator \mathbf{M} , as defined by $\langle \mathbf{u}, \mathbf{M}\mathbf{v} \rangle = \langle \mathbf{M}^*\mathbf{u}, \mathbf{v} \rangle$. Namely, \mathbf{M}^* is the transpose conjugate matrix of \mathbf{M} defined in Eq. 8. In our case, it can easily be seen that:

$$\mathbf{M}^* = -\frac{gH}{\Delta^*} \begin{bmatrix} -i\omega + r''''^* & f - r'^* \\ -f - r''''^* & -i\omega + r^* \end{bmatrix} \quad (25)$$

Once the adjoint system has been solved for η using Eqs. 22 – 24, the representer can then be determined by solving the following system (forward step):

$$S[r] = C_i[\eta] \quad (26)$$

with open boundary conditions

$$r = C_o[\nu + 1/\kappa\eta \cdot \mathbf{n}] \text{ on } \partial\Omega_o \quad (27)$$

and rigid boundary conditions

$$\mathbf{r} \cdot \mathbf{n} = 1/\kappa C_c[\eta] \text{ on } \partial\Omega_c \quad (28)$$

As with the direct hydrodynamic problem, the η and \mathbf{r} solutions are computed basin-wise, and the block resolution technique is used to obtain the global grid solution (see [Appendix](#)).

4 FES2004 atlas

The CEFMO model was initially developed for the shelf regions of the European seas and it was later extended for basin- and global-scale applications. The global tidal equations could not be solved at once with the best available computer national resources (vector super-computers at the *Institut du Développement et des Ressources en Informatique Scientifique*), and thus, the global tides were solved from basin-scale solutions with elevation boundary conditions mostly extracted from the NSW model and from the geodetic satellite (GEOSAT) empirical model (Cartwright and Ray 1991), and from tide-gauge data in dynamically complex regions such as the Indonesian Archipelago. The first global atlas released for the community was the FES94 and FES95 set. These global solutions were built from the separate basin solutions using a global optimal inversion method (inter-basin open boundary conditions optimisation in FES94, basin-wide variational assimilation in FES95), to which continuity conditions at the inter-basin open limits were added. Despite their remarkable accuracy, these atlases suffered from the limitations of the simplified assimilation

and continuity techniques used at that time. This problem was solved in 1997, with the development of the full variational assimilation code CADOR and a more effective block resolution technique (see [Appendix](#)). The FES98 atlas [tide gauge assimilation, Lefevre (2004)] and the FES99 atlas (tide gauge and altimetry assimilation) were produced using these improved methods, showing again a significant improvement compared to the previous atlases. A decision was made to refurbish the global mesh (from GFEM-1 to GFEM-2) and to produce a new global atlas. FES2002 was the first released atlas computed on of the GFEM-2 mesh. Unfortunately, the altimetric data assimilated in this atlas suffered from an improper inverted barometer correction that could have affected some tidal constituents, especially K_1 . To fix this problem and to take advantage of a better de-aliasing correction (MOG2D-G sea level simulations), the altimetric data were re-analysed and assimilated into the FES2004 atlas (Letellier 2004). Compared to the data assimilated in FES2002, the differences with the data assimilated in FES2004 are mainly concentrated in high-latitude regions, where the meteorologically forced sea surface variations are the most energetic. In addition, some data were removed from the assimilation set because of their strong contamination by non-tidal dynamics.

4.1 Description of the FES2004 tidal spectrum

Four main tidal constituents (M_f , K_1 , M_2 and M_4) plus S_1 are shown in Fig. 2. The digital FES2004 atlas (tidal elevation and loading/self-attraction) is available at the Laboratoire d'Etudes en Géophysique et Océanographie Spatiales web site, at <http://www.legos.obs-mip.fr/en/soa/>, in the “Sea level and tides” submenu. In the following sections, we will describe some specific aspects of the tidal components of the FES2004 atlas.

4.1.1 The diurnal and semi-diurnal tides

The main semi-diurnal and diurnal tides have been calculated using the CEFMO and CADOR codes: M_2 , S_2 , N_2 , K_2 , $2N_2$ and K_1 , O_1 , Q_1 , P_1 . The S_1 radiational tide was not computed for the FES2004 atlas, but is available from the FES99 atlas. The S_2 and S_1 components are discussed in detail below. To solve for the bottom friction non-linearities, M_2 and K_1 are computed within an iterative process until the M_2 and K_1 tidal currents converge, and hence, the bottom friction coefficients converge (typically, 10 iterations are needed to reach convergence, starting from a uniform M_2 tidal current of 1 m/s magnitude). After the hydrodynamic solutions are obtained with CEFMO, an assimilation is performed with the CADOR code with data from T/P and European remote-sensing satellite (ERS) crossover points, plus the harmonic analysis of tide gauge time series. Details of the assimilation will be given in section 4.2.

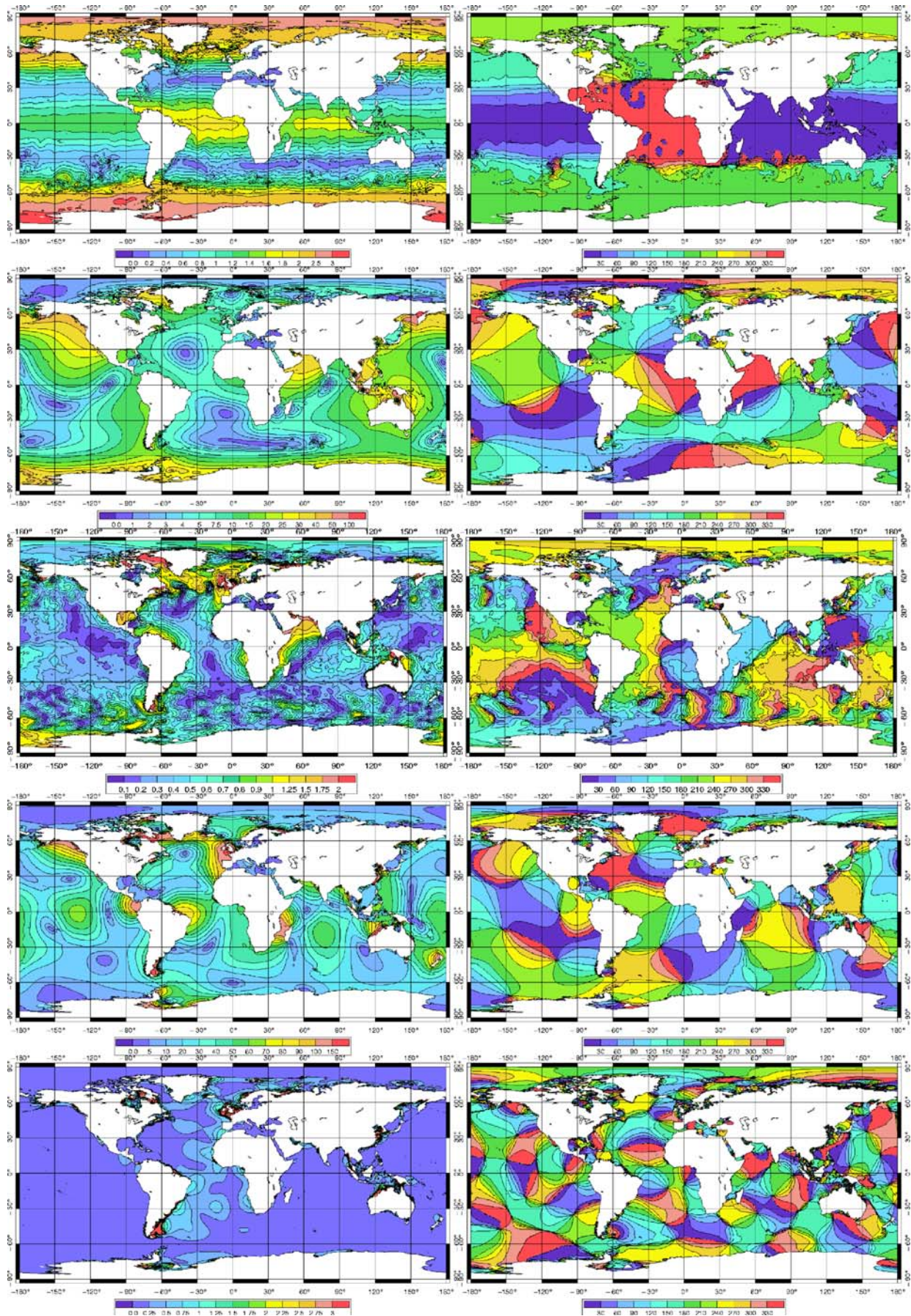
Fig. 2 From top to bottom, M_f , K_1 , S_1 , M_2 and M_4 FES2004 components. Amplitude (*left-hand side*) in metres, phase lag (*right-hand side*) in degrees

4.1.2 The long-period tides

For a long time, the long-period tides were modelled as equilibrium tides, which are the isostatic (or equilibrium) solutions of the tidal equations. This remains a good approximation, as their low frequencies will induce a weak dynamic ocean response to the gravitational forcing. Nevertheless, the presence of continents and the resulting transport barrier between the ocean basins is responsible for a slight departure of the true long-period tides from equilibrium, as demonstrated by Egbert and Ray (2003). Purely hydrodynamic models are able to capture, with reasonable accuracy, the dynamic parts of the long-period tides. In FES2004, no assimilation was performed for those tides. The reason is the unfavourable signal-to-noise ratio in the sea level observations in the long-period band, which contains a good deal of non-tidal ocean signals. The harmonic constants obtained from the analysis of those observations are meaningless except for the largest constituents in tropical regions (Ponchaut et al. 2001). Even in those low latitudes, the data are of poor interest for the assimilation, as they are significantly contaminated with non-tidal contributions. A good illustration of this problem is the unrealistic Schwiderski long-period atlas due to the nudging of the hydrodynamic solutions towards irrelevant data. Therefore, the four long-period tides distributed with the FES2004 atlas, namely, M_f , M_m , M_{tm} and M_{sqm} , are the solutions of the purely hydrodynamic CEFMO model.

4.1.3 The S_2 and S_1 tidal constituents case

Due to the thermal excitation by the solar radiation in the upper atmosphere, internal pressure waves are generated that propagate inside the atmosphere and down to the Earth's surface. The main high-frequency spectral lines (i.e. the ones which concern us in terms of de-aliasing) are the S_2 and S_1 atmospheric tides. The ocean response to the atmospheric tides, i.e. the ocean radiational tides, can reach several centimetres in amplitude in deep ocean regions, and even more on some continental shelf seas (some other astronomical constituents have a radiational contribution, such as K_1 , but it is usually considered as negligible compared to the gravitational contribution). Thus, those tidal constituents are far from negligible, and their contribution should be included in the tidal corrections. However, the surface pressure tides are not strictly constant in time, as both the excitation and the propagation of the atmospheric internal pressure waves can vary with time. The significant temporal variability of those tides means they should probably be removed from a spectral atlas and their correction left to atmospherically forced models (like MOG2D-G). Unfortunately, the time resolution of the



available global atmospheric surface field distributions [such as the European Centre for Medium-range Weather Forecasts (ECMWF)] is 6 h (at least for the operational analyses products). This allows an acceptable representation of the 24-h pressure oscillations, but is the exact Nyquist frequency for the S_2 atmospheric tide, making it appear as a stationary oscillation, whereas it should exhibit a westward propagation. Thus, ocean models with atmospheric forcing, such as MOG2D-G, contain an atmospherically driven semi-diurnal signal in their sea level fields, due to the partial atmospheric tide contribution at the 6-h periods of the ECMWF pressure fields. However, this signal is a distorted representation of the atmospheric forcing ocean response at this period. Further discussion on this radiational tide problem requires that we split S_2 and S_1 .

The S_1 tide is mainly composed of its radiational component, and its gravitational component can be neglected. Estimating S_1 using a spectral approach can be quite efficient, through either an empirical model or a hydrodynamic model with assimilation, in which the tidal forcing is obtained from a harmonic analysis of the atmospheric surface pressure. This provides a mean S_1 tide that is fitted over the time period from which the atmospheric tides and harmonic data have been extracted [such an approach was used to compute the S_1 constituent in the FES99 atlas using the harmonically analysed ECMWF operational analyses; see also Ray and Egbert (2004)]. In general, for spectral models, the overall accuracy of the global time-stepping hydrodynamic models is much better at the diurnal frequency than it is at the more resonant and dynamically dominated semi-diurnal frequencies. The S_1 tide can be simulated with reasonable accuracy from a purely hydrodynamic time-stepping model, such as MOG2D-G, as long as the atmospheric forcing data are themselves accurate. The authors strongly advocate for this approach in altimetric measurement de-aliasing. The use of a S_1 spectral component for de-aliasing purposes should be limited to data processing where the atmospheric loading effects are corrected by using an inverted barometer approximation instead of sea level elevations computed from a storm surge model.

The S_2 tide is composed of two contributions: one forced by the solar gravitational potential and one forced by the radiational one. In the open ocean, the radiational contribution is rather small, especially compared to the gravitational one, but it still can reach several centimetres, especially where the S_2 tide is amplified in the presence of the continental shelf. Unlike the S_1 case, the S_2 radiational component is badly represented in the MOG2D-G simulations due to the ECMWF products time sampling. In addition, the two S_2 components are undistinguishable in the sea level observations, whether altimetric or in-situ. As assimilation is mandatory to reach the required level of accuracy, it would be extremely difficult, and uncertain, to produce a purely gravitational S_2 solution. The most sensible choice consists of keeping both components

mixed into a unique S_2 solution where the radiational contribution comes from the use of sea level observations. Reconstruction of a “climatological” S_2 air tide can be used to improve the tidal forcing in the prior hydrodynamic model (Carrère 2003; Ray and Ponte 2003; Arbic 2005). Nevertheless, one must keep in mind that the time variability of this contribution would not be taken into account in the tidal corrections. Further investigations are necessary to estimate the impact of this time variability on the tidal correction error budget.

4.1.4 The M_4 tidal constituent

Due to the non-linearities in the tidal dynamics, extra constituents, called overtides or compound tides, are generated mainly on the continental shelves. The non-linear constituents can reach large amplitudes in these regions, and therefore attracted the attention of many authors, such as Le Provost and his fundamental contributions for the shallow water tides in the European shelf, especially in the English Channel (Chabert d’Hières and Le Provost 1978; Le Provost and Fornerino 1985). Most of those tides are barely significant in the open ocean, and are not considered to be needed to accurately predict the global ocean tides. Nevertheless, we have paid attention to these tides for two reasons: firstly, altimetry applications are being developed over the coastal regions and ocean shelves, and a precise tidal correction is needed. Secondly, the M_4 tide, due to the M_2 interaction with itself, is the most energetic compound tide in the global ocean, and is exceptional in the sense that we have evidence that it can reach a significant amplitude (about 5 mm to 1 cm) in some parts of the Atlantic Ocean. Due to its non-linear origin, the M_4 tide is quite tricky to model from the CEFMO spectral model. Assimilation is also a challenge. It can be extracted from altimetry only with great difficulty because of its weak amplitude and short wavelength (Andersen et al. 2006). It can be determined from coastal tide-gauge data, but this will generally reflect very local conditions that cannot be captured by the present resolution of global models, and thus are doomed to a large data representativity error. In the deep ocean regions, the M_4 tide amplitude is generally close to the observation noise level and, thus, rarely analysed. In summary, tide-gauge data that are appropriate for assimilation purposes are difficult to gather. Instead, we have used the MOG2D model to produce a M_4 tidal chart on the GFEM-2 mesh. It must be noted that the MOG2D basis functions are Lagrange-P1, where the CEFMO basis functions are Lagrange-P2, which means that the spatial resolution is twice as fine in the CEFMO simulations. However, comparisons between CEFMO and MOG2D simulations for the M_2 tide show a net advantage for the MOG2D runs, probably due to the better representation of the non-linear interactions in the time-stepping model.

4.2 Data assimilation

4.2.1 General case

The altimetry missions have brought to us the most synoptic observation network for tidal elevations, and one could designate the satellite altimetry missions as a global tide gauge system (Schrama and Ray 1994). Today, the accuracy of the empirical tidal models such as GOT00 [which is a follow-up of the GOT99.2 model; see Ray (1999)] far exceeds that of the purely hydrodynamic models for the global ocean tides, and most of the recent progress in tidal science is directly or indirectly linked to the tidal analysis of satellite measurements. Nevertheless, some characteristics tend to limit the accuracy of such analyses. The major drawback comes from the aliasing of the tidal frequencies due to the poor repetitivity of the satellite missions. For a given constituent, its apparent frequency projects into the low frequency part of the ocean spectrum (including the zero frequency, as is the case for the S_2 and S_1 tides in a sun-synchronous mission). The aliased tidal components get mixed up with non-tidal signals (thus penalising the analysis of small-amplitude tidal constituents). The aliased frequency can also be very close to another tidal-constituent-aliased frequency, yielding unusual tidal separation problems (such as the 10 years required to separate K_1 and S_{sa} in the T/P time series). The use of admittance or ortho-tide techniques (Groves and Reynolds 1975; Munk and Cartwright 1966) can partially improve the analysis problem, as well as the use of the crossover doubled time series. In fact, the tidal analysis needs to be carefully chosen and tuned for each satellite mission, and the accuracy will be quite heterogeneous from one tidal constituent to another and from one satellite mission to another. Additional errors can arise from internal tide, which can generate a significant surface signature (which can reach a few centimetres for the M_2 tide in numerous regions of the global ocean), or when the tidal distribution shows structures with scales of the order of 100 km, as can be found in shelf and coastal seas.

For the FES2004 atlas, the assimilated data set is composed of 671 tides gauges (Fig. 3a), plus 337 T/P (Fig. 3b) and 1,254 ERS (Fig. 3c) altimetric crossover points. The locations of these data sets are similar to the FES2002 assimilation, except that some altimetric points have been removed where the harmonic analysis is badly damaged by strong non-tidal sea level signals (two T/P data sites in the southeast Indian Ocean, one T/P data site in the Gulf Stream and one ERS data site along the Somali coastline). A tidal spectrum with 20 constituents was analysed for all the T/P altimetric data and a tidal spectrum with 19 constituents for the ERS data (S_2 constituent excluded, see Section 4.2.2). A direct harmonic analysis was performed in the case of T/P data and a generalised admittance algorithm for the ERS data (i.e. additional constraints based on the assumption of the ocean response smoothness in frequency space, similar to the ortho-tide method). As stated earlier, the major difference between the FES2002 and FES2004 solutions is the de-aliasing

correction used before the tide analyses of the altimetric data. An alternative correction was used instead of the classical inverted barometer. MOG2D-G is a modelled estimate of the sea surface response to both the atmospheric pressure and the wind forcing. It has already demonstrated its capacity to reduce the altimetric signal variance (Carrère and Lyard 2003). MOG2D-G has been chosen by the Ocean Surface Topography altimetric community as a standard de-aliasing correction of the sea-level response to the atmospheric forcing. MOG2D-G is needed to remove high frequencies due to the atmospheric forcing, aliased at the same frequencies as the tidal frequencies. Using this correction leads to some significant changes in the results of the harmonic analyses, especially in the middle to high latitudes, where the sea level variability due to the atmospheric forcing is larger (Fig. 4). For the M_2 constituent, the differences observed in the North Atlantic Ocean are about 2 cm for the T/P data and more than 4 cm for the ERS data (which have more points located over the shelf seas and along the coasts).

4.2.2 Assimilation of the S_2 tidal constituent

As stated earlier, the S_2 tide is composed of two contributions: the solar gravitational potential tide and the radiational tide. This particularity implies a different treatment for the assimilation procedure, compared to the other astronomical constituents. Firstly, ERS1 and ERS2 have a sun-synchronous orbit, so that the S_2 tidal constituent appears as a locally constant sea level contribution in the satellite observations, and thus, cannot be directly analysed harmonically. The ortho-tide or generalised admittance harmonic analysis, which, in theory, allows us to extract a S_2 component from the ERS1/2 data, did not yield sufficient accuracy, especially in the shelf and coastal regions where the smoothness assumption is less justified. In addition, mixing the gravitational and radiational contributions is known to degrade this approach, as it depends on tidal gravity potential considerations only. Thus, no ERS1/2 data are assimilated in the FES2004 solution for the S_2 constituent. ERS1/2 data were also discarded from the assimilation in the FES2002 K_2 solution, as they appeared to be of poor accuracy (which may have been a side effect of the S_2 analysis problem in ERS). By mistake, ERS1/2 data were included in the FES2004 atlas computation of the K_2 tide. Our recommendation is *to use the FES2002 K_2 instead of the FES2004 K_2 tidal elevation solution.*

Secondly, specific processing is also needed for the T/P altimetric data before tidal analysis. The S_2 semi-diurnal signal was removed from the MOG2D-G correction using a harmonic analysis. Consequently, the harmonic analysis of the T/P data, corrected with MOG2D-G, includes the full S_2 radiational contribution, as measured by the altimeter. This is also the case for the tide-gauge data, which need no specific correction before the tidal analysis, except for the bottom pressure gauge data, which need an atmospheric pressure correction to

Fig. 3 **a** Positions of the 671 tide-gauge data assimilated. **b** Positions of the 337 T/P crossover data assimilated. **c** Positions of the 1254 ERS crossover data assimilated

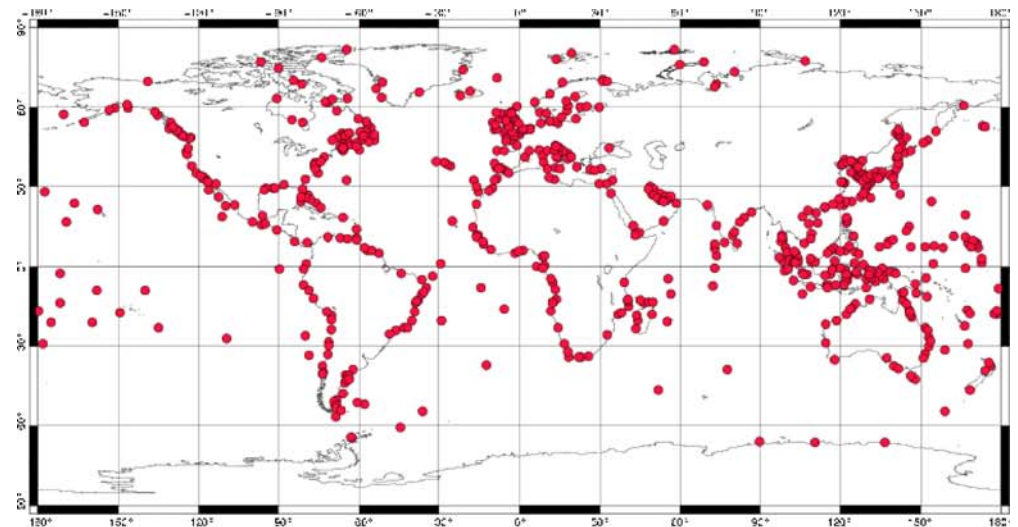
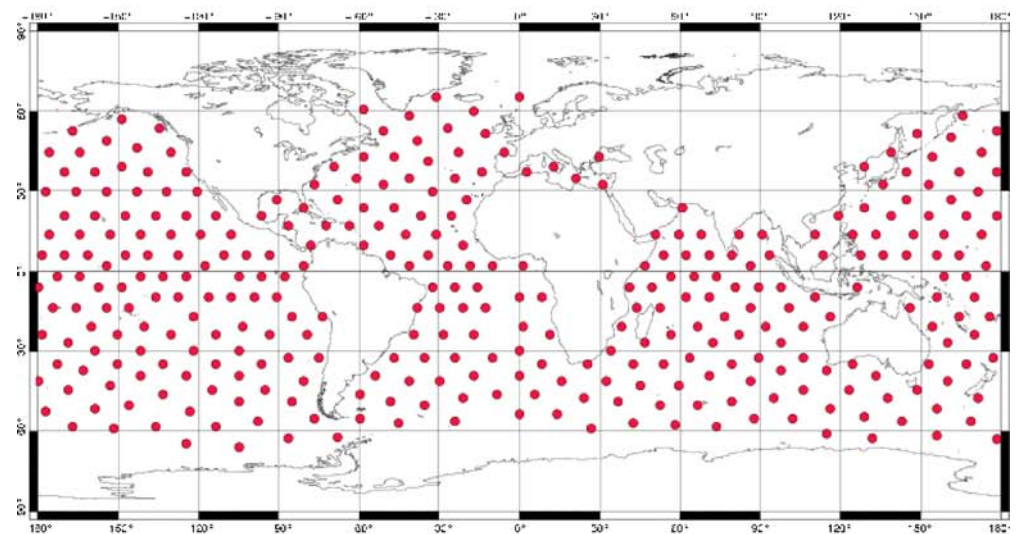
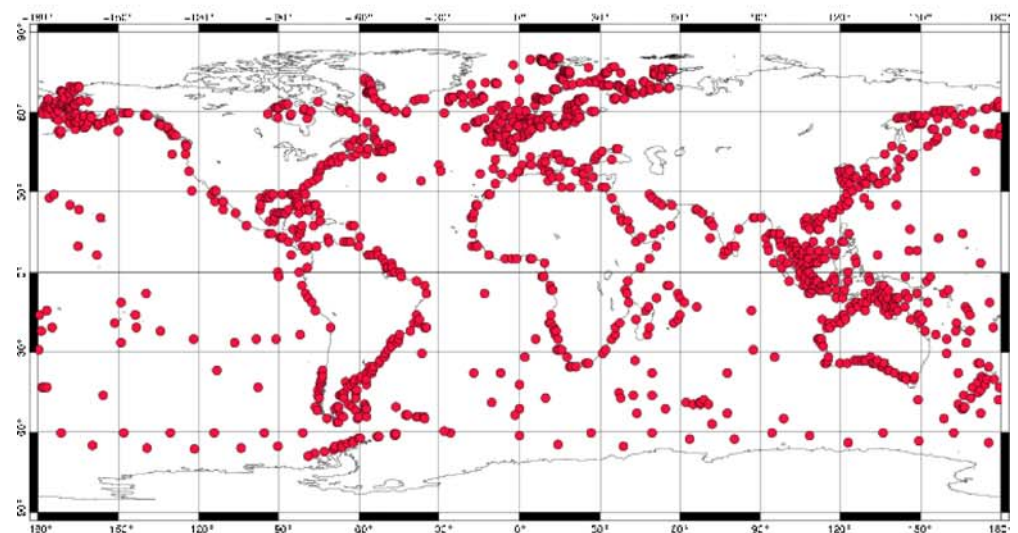
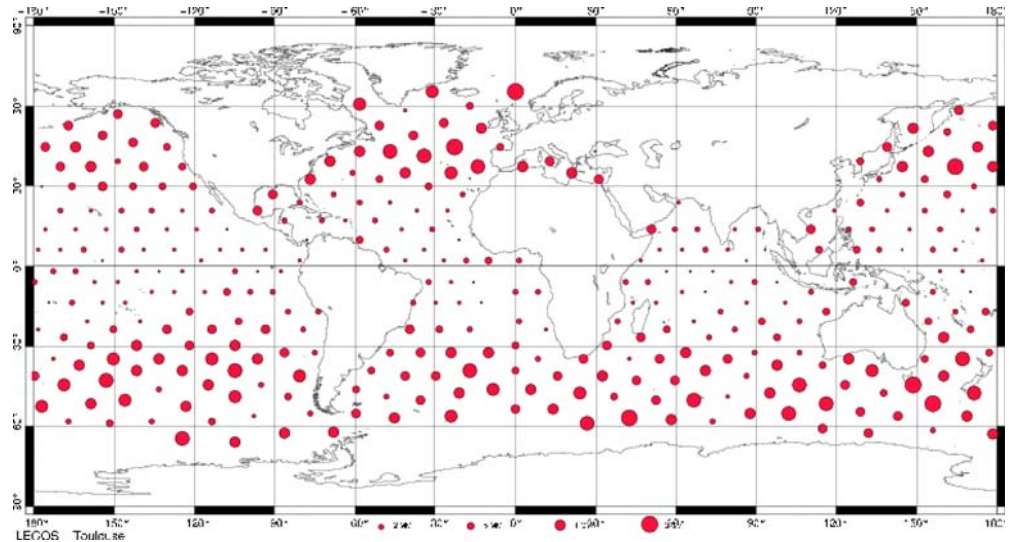
**a****b****c**

Fig. 4 Difference for the K_2 constituent between tide analyses of T/P data correction with MOG2D-G or with the inverted barometer. The *circle* surface is proportional to the difference, about 1 mm in the central and about 1.5 cm in the southern Atlantic Ocean



convert pressure measurements into sea level data [such correction is usually already done by the data providers for the coastal tide gauges; it is, unfortunately, not the case for deep ocean data, such as the International Association of the Physical Sciences of the Ocean (IAPSO) data set]. The CEFMO model used to compute the hydrodynamic solution is forced with the gravitational potential and does not include the radiational component of the S_2 tidal constituent, but after the assimilation process, the FES2004 solution fully includes the radiational component of the semi-diurnal S_2 constituent.

4.3 Validation against tide-gauge data

Because most of the available valuable tide-gauge data have been assimilated in the FES2004 solutions (except for the IAPSO data set), it is impossible to perform a totally independent validation using tide-gauge data. Instead, three tide-gauge data sets have been arbitrarily chosen for the comparisons. The first two were chosen because of their high quality: the world ocean circulation experiment (WOCE) data set composed of about 400 tide gauges located along the coasts and on islands and the IAPSO data set consisting of 352 tide gauges located in deep ocean regions especially in the North Atlantic and Pacific Oceans. The third one is the ST102 tide-gauge data set, with data mostly located in the deep ocean. It is the historical database used to evaluate the T/P project tidal models (Shum et al. 1997). Again, the ST102 and WOCE data have generally been used in FES2004 data assimilation, and not the IAPSO database (except for the IAPSO data selected in the ST102 data set). Model–data comparison scores for these three data sets were computed for the main tidal constituents and are presented in Table 1. The GOT00 empirical tidal model [which is a follow-up of the GOT99.2 model; see Ray (1999)] has been included in the comparison to provide an external reference.

The performance of the three tidal models is very similar in comparison to the ST102 data set, which indicates that they are very similar on average over the world's deep oceans. The same conclusion can be drawn from the IAPSO data set. The differences are more significant on the

Table 1 The global mean rms difference of the tidal models against tide-gauge data sets, as explained in the text

| Model | Wave | IAPSO | WOCE | ST102 |
|---------|------|-------|------|-------|
| FES2004 | | 3.8 | 8.5 | 1.7 |
| FES2002 | M2 | 3.9 | 9.7 | 1.7 |
| GOT2000 | | 4.6 | 11.1 | 1.6 |
| FES2004 | S2 | 2.2 | 4.4 | 1.0 |
| FES2002 | | 2.2 | 4.8 | 1.0 |
| GOT2000 | | 2.3 | 5.3 | 1.1 |
| FES2004 | N2 | 1.1 | 2.2 | 0.7 |
| FES2002 | | 1.1 | 2.5 | 0.7 |
| GOT2000 | | 1.1 | 2.4 | 0.6 |
| FES2004 | K2 | 0.9 | 3.0 | 0.5 |
| FES2002 | | 0.9 | 2.1 | 0.5 |
| GOT2000 | | 0.9 | 1.7 | 0.4 |
| FES2004 | 2N2 | – | 0.6 | 0.3 |
| FES2002 | | – | 0.7 | 0.2 |
| GOT2000 | | – | – | – |
| FES2004 | K1 | 1.4 | 2.7 | 1.0 |
| FES2002 | | 1.5 | 2.7 | 1.0 |
| GOT2000 | | 1.4 | 2.8 | 1.0 |
| FES2004 | O1 | 1.0 | 1.9 | 0.8 |
| FES2002 | | 1.1 | 1.9 | 0.8 |
| GOT2000 | | 1.3 | 2.0 | 0.8 |
| FES2004 | Q1 | 0.5 | 0.5 | 0.3 |
| FES2002 | | 0.5 | 0.6 | 0.3 |
| GOT2000 | | 0.5 | 0.5 | 0.3 |
| FES2004 | P1 | 0.5 | 1.0 | 0.4 |
| FES2002 | | 0.4 | 1.1 | 0.4 |
| GOT2000 | | 0.4 | 1.0 | 0.4 |

Units are in centimetres

WOCE data set and the discrepancies are (not surprisingly) amplified in coastal regions. The comparison shows an improvement in FES2004 compared to FES2002, except for the K_2 tide (see above section). To further highlight the differences between FES2002 and FES2004, it would be necessary to show regional comparisons all over the global ocean, as is the general case for all the best recent tidal models. This is far beyond the scope of this paper (focusing on global aspects), and therefore will be left to future publications on regional applications.

4.4 Validation against altimetry data

To further validate the accuracy of the FES2004 atlas at the global scale, we compare the associated tidal prediction against sea level altimetric measurements. Though the main tidal constituents computed within the FES2004 atlas (hydrodynamic/assimilation solutions) represent the prominent part of the tidal spectrum, one must consider the importance of the other tidal constituents of smaller amplitude (such as Mu_2 , Nu_2 , $2Q_1$, etc.), whose individual contributions are small but become significant when added together. Consequently, additional semi-diurnal and diurnal constituents were deduced from a spline and linear admittance method (described by Cartwright and Spencer 1988; Le Provost et al. 1991; Lefevre et al. 2002) and added to the prediction spectrum. To compute the geocentric tides that will be compared with altimetry data, it is necessary to include the ocean bottom vertical displacement resulting from the solid Earth tide and the tidal loading. The solid Earth tide can be easily deduced analytically from the astronomic potential, but the tidal loading needs to be computed from an ocean tide model. At the time of writing this paper, the computation of the loading effects derived from FES2004 was not yet completed, and the loading effects deduced from FES99 are used for validation against altimetry.

The archiving, validation and interpretation of satellite oceanographic (AVISO) data processing chain has been used to study the reduction of the standard deviation in sea level when the different tidal corrections are applied (all other corrections being identical) for two subsets of altimetric data [Jason-1 and environmental satellite (ENVISAT)]. The FES2004 correction is compared with the best former FES model, namely, FES99 (where coastal and pelagic tide-gauge data and deep ocean T/P and ERS data were assimilated). Both atlases contain the same tidal constituents. We consider that a lower standard deviation (or the variance) reflects a better tidal model. Note that these two altimetric data sets are not assimilated in the

FES99 and FES2004 solutions. For Jason-1, we consider cycles 001 to 101 (10 January 2002 to 3 October 2004), and for ENVISAT, cycles 011 to 031 (5 November 2002 to 5 October 2004). Nearly 3 years of data are taken into account for Jason-1 (2 years for ENVISAT). Over such a time span, the contribution of long-period tides (such as M_f or S_a) or tides aliased on a long period (like K_1) will be detectable in our comparisons. More generally, the time period is long enough to provide statistically significant information on the tidal model accuracy. The altimetry data are used in two ways: First, computations are made at crossover points especially to demonstrate the improvements yielded by FES2004 in coastal areas. Second, statistics are calculated on along-track data so as to provide an overview of the quality of FES2004 on the global scale.

4.4.1 Standard deviation reductions at crossover points

For each Jason-1 cycle, about 4,000–8,000 (25,000–50,000 for ENVISAT) crossover points are available for comparisons. The difference in the number of points is the consequence of the orbit characteristics of the two satellites and the numerous corrections applied before calculating sea surface heights from the altimeter data. The main defect of FES99 was located in shallow water and coastal areas. Tests with crossover points are undertaken to demonstrate the improvements of FES2004 in such areas. Three estimates are performed. The first estimate uses the global sets of crossover data. The second estimate only considers crossover points located in the deep ocean (at depths greater than 1,000 m). The third estimate considers crossover points in shallow water and coastal areas (at depths lower than 1,000 m). The comparison results (Table 2) demonstrate the better performances of FES2004 on the global scale. Compared to Jason-1 data, FES2004 is 12.0% (7.1% for ENVISAT) better than FES99. However, these overall improvements are mainly due to the improved accuracy of FES2004 tidal constituents in coastal and shelf areas where it is 30.1% better than FES99 for Jason-1 (23.4% for ENVISAT).

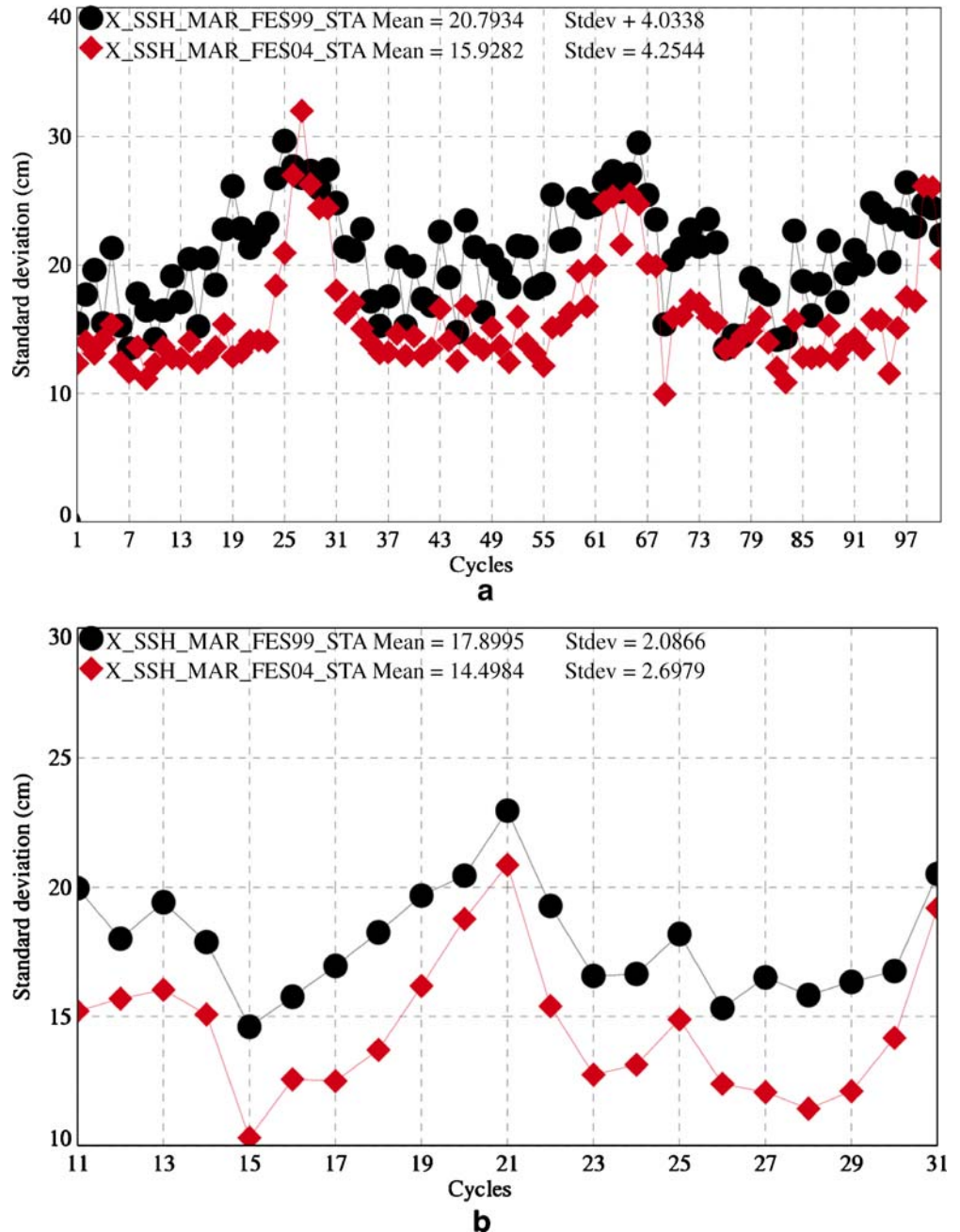
These results are confirmed if we look at the standard deviations calculated cycle by cycle for the two FES models for Jason-1 and ENVISAT in shallow water. Indeed, very few Jason-1 cycles showed larger residual standard deviations for FES2004 than for FES99 (Fig. 5a). However for ENVISAT, which provides nearly 10 times more data in shallow water than Jason-1, FES2004 always performed better than FES99 for the 21 considered cycles of the satellite (Fig. 5b). The complete set of results at

Table 2 Reduction in standard deviation at crossover points

| Satellite | Solution | Global ocean | Depth>1,000 m | Depth<1,000 m |
|-----------|----------|--------------|---------------|---------------|
| Jason-1 | FES99 | 9.3 | 6.8 | 20.8 |
| | FES2004 | 8.3 | 6.8 | 15.9 |
| ENVISAT | FES99 | 10.6 | 8.8 | 17.9 |
| | FES2004 | 9.9 | 8.8 | 14.5 |

Units are in centimetres

Fig. 5 a Jason-1 SSH crossover standard deviations for FES2004 (*red*) and FES99 (*black*) for shallow water (depths less than 1,000 m). Units in centimetres.
b ENVISAT SSH crossover standard deviations for FES2004 (*red*) and FES99 (*black*) for shallow water (depths less than 1,000 m). Units in centimetres



crossover points leads to the conclusion that FES2004 performs better in coastal areas without decreasing the accuracy in the deep ocean when compared to FES99.

4.4.2 Standard deviation reduction along tracks

In addition to the crossover analysis, a huge amount of altimetry data is also available along track: about 400,000 data points per cycle for Jason-1 and about 1,400,000 for ENVISAT. This allows for highly valuable statistical studies of the along-track standard deviation reduction. For the two satellites, the variances of the altimetric residuals were computed with exactly the same geophysi-

cal data record corrections, except for the tidal corrections (either FES99 is used or FES2004). The difference between the two sets of sea level anomaly (SLA) variance is shown in Fig. 6a for Jason-1 and in Fig. 6b for ENVISAT. The blue colours in the maps correspond to lower sea level variances when corrected with FES2004 rather than FES99 correction. The differences are around 0 ± 0.05 cm. Areas shaded light green to yellow highlight the locations where FES2004 and FES99 perform almost the same (essentially, the deep ocean).

The main differences occur in coastal areas and continental shelves. These areas are mainly in deep blue (variances lower than 1 cm^2), which means that FES2004 correction performs better than FES99 (Indonesian Seas,

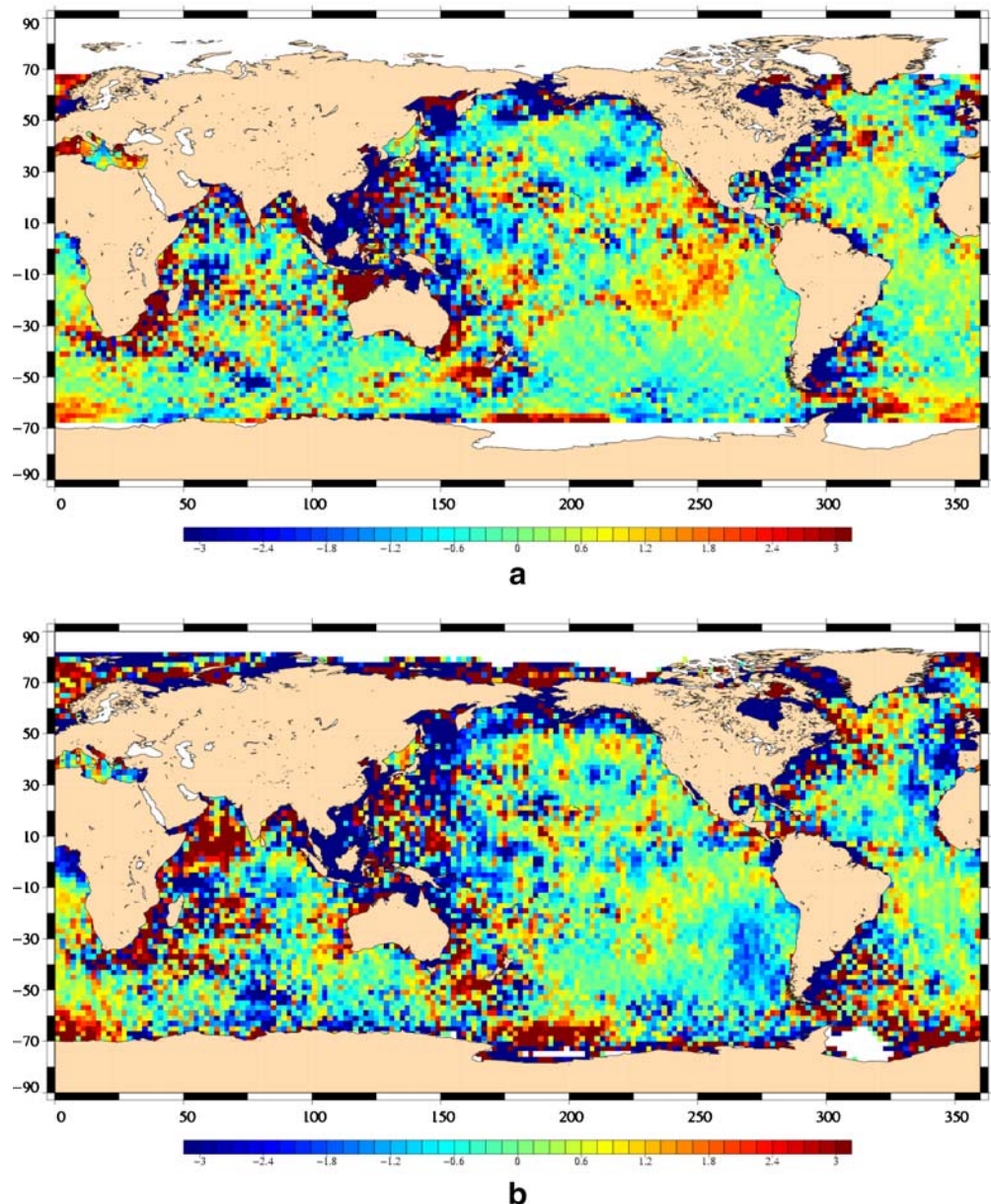
China Seas, Okhotsk Sea, Aleutian Islands area, Hudson Bay, Patagonian shelf, east and west coasts of the Atlantic Ocean...). These results are similar for Jason-1 and ENVISAT, and confirm the results of the crossover studies. Depending on the satellite, several areas are coloured in deep red (variances higher than 1 cm^2): FES99 performs better in these locations (for Jason-1: northeast coast of Australia, eastern part of the equatorial Pacific Ocean, some parts of the Antarctic Ocean; for ENVISAT: the Arabian Sea, some parts of the Antarctic and Arctic Oceans). We do not have an explanation for these observations, but we make two points. First, the assimilation scheme is quite complex to adjust at the global scale because one data assimilated in a given location can modify the tidal solution at the other side of the world ocean (typically, the open ocean data representers show, at least, basin-wide correlations). Second, the loading effects used

for tidal corrections are computed with the LSA deduced from FES99. Consequently, they are not fully coherent with the FES2004 tidal elevations (contrary to FES99 elevations). However, the FES2004 achieves its main purpose: improving the previous best available FES atlas (FES99) in coastal areas and on continental shelves while keeping the best possible accuracy in the deep ocean.

4.5 FES2004 LSA atlas

The loading radial deformation and gravity potential perturbations have been recently computed from the FES2004 atlas gridded fields (by opposition to the finite element fields). The overall distribution of these terms is very similar to that computed from the FES99 atlas. Nevertheless, significant differences appear in coastal and

Fig. 6 **a** Difference of variances between FES2004 and FES99 along Jason-1 tracks. Units are in centimetres squared. **b** Difference of variances between FES2004 and FES99 along ENVISAT tracks. Units are in centimetres squared



shelf regions. The first reason for this is the difference in the tidal elevations themselves. The second reason, and probably the more significant, is the grid resolution used to compute the LSA maps. The FES99 mesh has an average 10-km-alongshore resolution, whereas the FES2004 has a 7.5-km resolution. However, the FES99 atlas was projected onto a 0.25-degree grid for distribution, whereas the FES2004 was projected onto a 0.125-degree grid. The finer horizontal scales at the ocean and continental limits are thus much better captured in the FES2004 SLA atlas. For example, the complex difference between FES99 and FES2004 SLA is very large at the entrance of the English Channel. In the Northeast Atlantic, both SLAs show similar, large values due to the open ocean tide influence, which later decrease rapidly upon entering the English Channel because of the diminishing wet/dry land ratio. The SLA distribution seen in this region is strongly affected by the tidal model details and resolution and differs significantly between FES99 and FES2004. In a hydrodynamic model, this effect will be amplified by the small horizontal scale of the discrepancy because the dynamic forcing contribution is the gradient of the SLA field. Improving the SLA resolution thus leads to a better coastal tide solution in regions such as the European shelf, with an impact on the global scale if the tidal currents and dissipation are significantly modified in those areas.

5 Tidal dissipation

Initially developed during the 1970s for the shelf regions of the European seas, the CEFMO model was specially designed to deal with coastal ocean conditions. Despite a spectral formulation, the wave-to-wave non-linear interactions are carefully taken into account within the quasi-linearisation of the shallow water equations. In particular, the bottom friction terms have been developed under the assumption of the existence of a dominant tidal wave (in terms of the tidal current magnitude). The model discretisation is based on a finite element grid that allows us to modulate the grid resolution as a function of the local dynamical constraints. Although the primary objective is to establish the best possible global tidal elevation solution, the correct representation of the tidal dissipation is also a major priority. This implies having enough accuracy in regions of strong dissipation, but also implies including all of the dissipation regions, including the Weddell Sea. Modelling of this region, which is mostly covered by a thick, permanent ice-shelf, has demanded a tedious, but worthy, effort to compute the thickness of the free seawater located between the bedrock and the bottom of the ice shelf (Genco et al. 1994). Although appropriate bottom friction has been implemented, the global tidal energy budget of the FES99 assimilation solutions has highlighted worrying anomalies, especially for tidal dissipation (Le Provost and Lyard 1998).

However, due to the coherence of the numerical model, the energy budget of the FES hydrodynamic solutions is fairly balanced. Considering the case of the M_2 component,

the rate of work of the astronomical potential forces was found to be close to the well-constrained global total value of 2.45 TW. However, the rate of work of total bottom friction turned out to be too small (about -2.1 TW). Inversely, the estimated total LSA rate of work (which should be zero when integrating over the whole ocean) reached an unphysical significant value compared to the global budget (about -300 GW for the M_2 component), compensating for the lack of dissipation. The reason for these anomalies is the inconsistency between the prior tidal elevation used to compute the LSA, and the actual model solution, but this inconsistency itself is probably linked to the dissipation problem. A series of simulations was carried out to tune the bottom friction coefficient over a large range of values, globally and regionally. The overall results showed very limited changes in total dissipation, whereas the solutions were degraded when the non-dimensional friction coefficient in Eq. 1 departs significantly (by an order 10) from the usual value of 2.5×10^{-3} . The conclusion is that the bottom friction cannot compensate for the lack of dissipation.

Estimating the energy budget of the M_2 FES99 assimilated solution is much trickier. The output of the assimilation code CADOR is a tidal elevation solution. Retrieving the velocity field cannot be done directly by applying the momentum equations; instead, one needs to solve an over-determined system that includes the continuity equation, with a misfit associated with each dynamical equation. Even so, no satisfactory velocity field could be obtained. The rate of work of the total pressure forces constantly shows a significant non-zero value (about 0.6 TW for the M_2 component) due to pathological current determination (whereas the SLA rate of work was close to zero). In summary, the hydrodynamic model lacked dissipation, while a consistent velocity field could not be found for the assimilated solutions, showing the lack of some physics in our model.

In separate work, evidence of internal tides that are ubiquitous in the world oceans was demonstrated from the analysis of T/P along-track measurements (Ray and Mitchum 1996). These observations renewed the question about how much of the barotropic tidal energy is converted into internal tides and indicated that the conversion might be significant. The observed surface signatures of the internal tide have wavelengths comparable with the first internal mode wavelength computed from the Levitus climatology (Carrère et al. 2004). The internal waves appear to be generated from the largest topographic slopes, such as the Hawaiian volcanic ridge, then propagate until they reach regions with a strong stratification contrast, such as the equatorial band or the subtropical gyre front, where their surface signature vanishes. Intriguingly, the maximum hydrodynamic inconsistency (between the FES99 assimilated elevations and tidal hydrodynamic equations) was found at the same ocean ridge slopes. These facts encouraged us to investigate the problem of barotropic tidal energy dissipation through internal wave generation processes.

As the CEFMO model is a depth-averaged barotropic model, we cannot use it to solve the 3D internal ocean dynamics, so a parameterisation has to be added to account for the internal wave drag. A great deal of theoretical work has been dedicated to this issue, with a recently renewed interest in the matter. In short, the various specific approaches and the necessary prior assumptions restrain the field of validity of the proposed parameterisation. For instance, in the case of small topographic structures (i.e. typical horizontal lengths smaller than the local tidal excursion), the following parameterisation can be found with more or less sophisticated forms in classical literature (see Jayne and St. Laurent 2001; Lewellyn Smith and Young 2002; Egbert et al. 2004):

$$\tau_1 = c_1 \rho_0 \frac{\kappa}{\omega} [(N_b^2 - \omega^2)(\omega^2 - f^2)]^{\frac{1}{2}} h^2 \mathbf{u} \quad (29)$$

where N_b is the Brünt–Vassala frequency at the ocean bottom, κ the typical topography horizontal wave number, h the typical topography vertical dimension, ω the tidal wave frequency, f the Coriolis factor and \mathbf{u} the barotropic velocity. c_1 is a tuning coefficient which accounts for parameterisation uncertainties, such as the N_b estimate or the inadequacy of the model resolution above topographic features. This parameterisation is valid for topographic scales that are typically of the order of O (1,000 m) and less. From altimetry observations, the main sources of internal waves are located on much larger topographic structures, such as volcanic ridges, and an original parameterisation was designed for the barotropic models, such as CEFMO, to deal with the large topographic scales:

$$\tau_2 = c_2 \rho_0 \frac{\kappa^{-1}}{\omega} [(N^2 - \omega^2)(\omega^2 - f^2)]^{\frac{1}{2}} (\nabla H \cdot \mathbf{u}) \nabla H \quad (30)$$

where H is the ocean mean depth and N a depth-weighted average buoyancy frequency, with weights decreasing linearly from bottom up to the surface to account for the vertical velocity upward linear decrease. Despite the fact that it was derived by using a different approach, this parameterisation can be seen as a simplified version of the parameterisation proposed by Bell (1975). The major difference with the first parameterisation in Eq. 29 is that the wave drag has the direction of the topography gradient and not the direction of the barotropic current. Sensitivity experiences have shown that this second formulation was better suited for the observed energy transfer.

Two independent experiments were used to calibrate the tuning coefficient c_2 in Eq. 30 and its impact on the M_2 wave energy budget. The first experiment retrieved the velocity field associated with the FES99 assimilated elevations, with the objective of reducing the global rate of work of pressure forces to zero. In the second experiment, we recomputed a hydrodynamic solution (using GFEM-2 mesh) with the objective of minimising the misfits with the ST95 tidal constants data set. The

resulting spatial distribution of the wave drag and bottom friction dissipation, similar in experiments 1 and 2, are shown in Fig. 7 and Fig. 8. Both experiments led to the same dissipation estimate, i.e. 1.8 TW bottom friction dissipation and about 0.7 TW internal wave drag dissipation, with a spatial rate of work distribution that is extremely coherent with the satellite altimetry observations of internal wave generation. These estimates are also close to those from other tidal groups (Egbert and Ray 2001). In addition, the averaged M_2 FES hydrodynamic solution discrepancy was divided by a factor of 2 (from 12 cm rms down to 6 cm rms when comparing with the ST95 tidal constant database) when the wave drag parameterisation was applied. Contrary to the bottom friction dissipation, which is confined to some limited shelf regions, the wave drag dissipation is widely spread in the ocean and can be the dominant dissipation mechanism in basins where the continental shelves are of relatively small extent, such as the Indian Ocean.

As a conclusion, the proportion of M_2 barotropic tidal energy dissipated through the internal wave generation is about 0.7 TW, or roughly 25–30% of the total M_2 barotropic energy dissipation. Approaching or similar numbers were obtained using different approaches (10% in Bell 1975; 25% in Morozov 1995). The parameterisation of this energy sink is a key point in global tidal hydrodynamic modelling. Many authors have recently examined the problem, including Egbert et al. (2004), who used a paleo-tidal simulation experiment, but further developments are needed to improve the performance of the present schemes. Simmons et al. (2004a,b) have recently investigated the M_2 baroclinic tide from an idealised 3D model (i.e. with a uniform stratification), showing the dominance of the first baroclinic mode as it would be expected from the altimetry observations analysis (still, one must keep in mind that possible higher-order modes would be much more difficult to observe from altimetry, as their surface signatures will show much smaller wavelengths). Their energy conversion budget is similar to that provided in this paper and in other recent studies; however, they underlined the limitation of their experiment. In particular, the energy balance between the energy captured over the large topographic features such as the Hawaii archipelago, or submarine rugged structures such as ocean ridges, was found to be highly dependent on the number of vertical layers in their model. Also, the dissipation of the baroclinic tides was poorly resolved. For instance, the baroclinic waves propagating from the Tuamotu Islands do not “feel” the equatorial band crossing, whereas the altimetry observations indicate a dissipation or a strong modification of the internal wave regime. In their two layer experiments, the baroclinic tide energy was converted back into barotropic energy at a rate (−0.73 TW) comparable to the total barotropic/baroclinic energy conversion budget (+0.67 TW). This could result from the lack of a dissipation mechanism for the internal waves, and therefore, may vanish in a more realistic simulation. The difficulty in undertaking more accurate experiments is due to the high computational cost of a global, internal tide

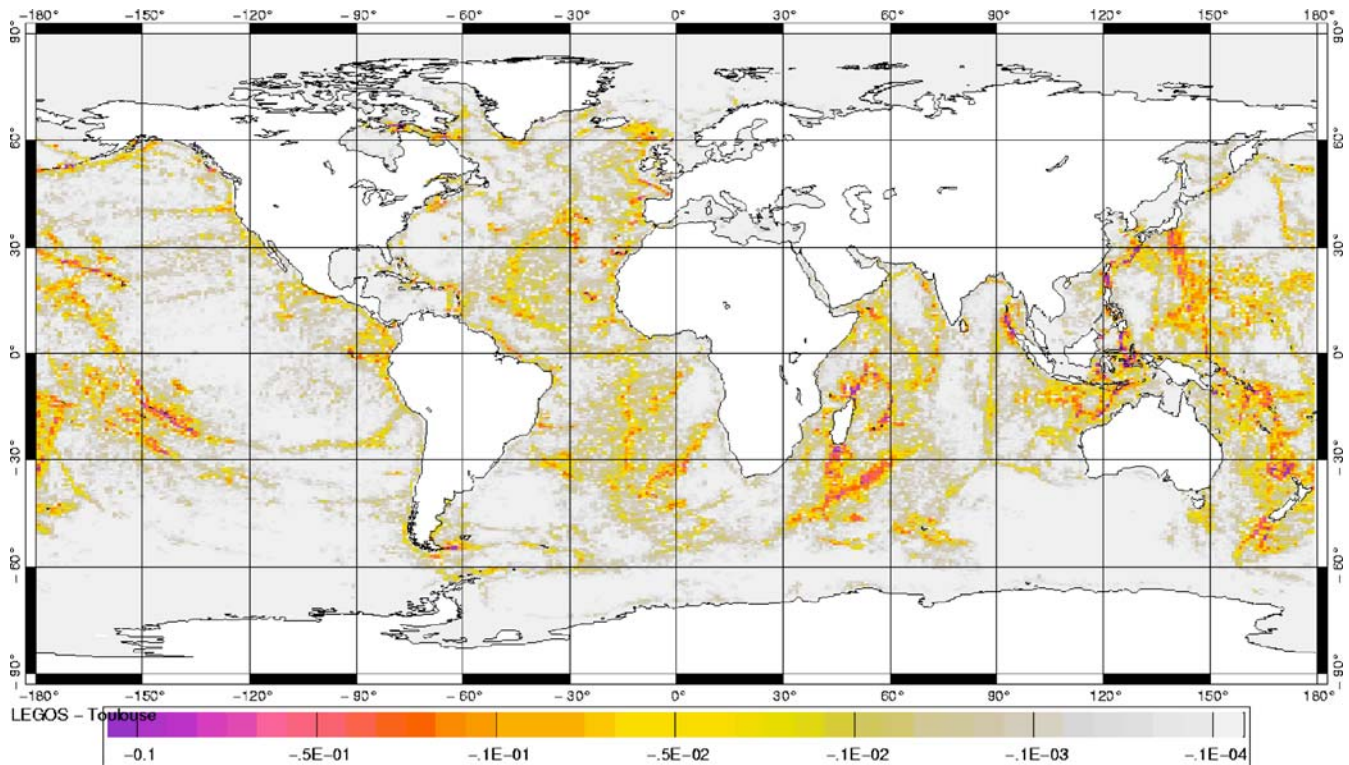


Fig. 7 M_2 wave drag dissipation (W/m^2)

model, especially if realistic stratification is to be taken into account. Nevertheless, because of the possible role of the internal tide in the ocean mixing (as described by Munk and Wunsch 1998), the ocean circulation and tidal communities have now joined forces to investigate this important matter. Because the simultaneous resolution of the ocean circulation and tidal dynamics requires huge computational power (mainly because of the reduced time step and the need for sub-kilometric horizontal resolution), the first step is to parametrise the tidal effects in ocean circulation models and the stratification effects in tidal models. Both analytical and numerical attempts have been carried out, on global (Simmons et al. 2004a,b; Bessières, personal communication) or regional scales. Improvements in our comprehension and quantitative estimates of barotropic to baroclinic energy conversion will allow major improvements in future tidal hydrodynamic models.

6 Conclusions

Much progress has been made during the past 15 years in the field, and our present knowledge of deep-ocean and coastal tides is considerable compared to what it was before the altimetry satellite missions. Not only are the tides now precisely known in the global ocean, but we also have learned and quantified new aspects of tidal dynamics. The FES2004 atlas is the last and most accurate of the FES atlases. Its performance is slightly improved in the deep ocean regions, and more significantly in the shelf and coastal areas (except for the K_2 component, which should

be taken from the FES2002 atlas). However, the spectral approach has probably reached its limits with the FES2004 atlas. It also seems very difficult now to continue to globally improve tidal models, at least in the deep ocean, as their accuracy is bounded by the altimetric data error budget and analysis limitations. For instance, the presence of non-tidal ocean dynamics and internal waves, which create a high-frequency surface signature, is an obstacle to improving our data assimilation results, or indeed to including minor tidal constituents in the assimilation list with sufficient confidence. Further steps based on the same approaches as those developed during the last 15 years would probably lead to minor changes in the global tidal model solution but at an unsustainable cost.

Still, the tidal challenge has not yet ended. The next-generation models will need to improve the tidal solutions in the coastal and shelf regions, with the objective of narrowing the gap between the deep ocean and shallow water range of prediction accuracy. At the first step, regional hydrodynamic models are needed to study and solve properly the local, strongly non-linear dynamics over the ocean shelves. In such regions, it is the authors' opinion that assimilation cannot be the ultimate answer, firstly because data are much sparser relative to the tidal wavelength, and secondly because the tidal spectrum must be extended to the non-linear constituents which are barely observed with altimetry. Indeed, the accuracy of the present atlas FES2004 relies very much on the data assimilation and does not truly represent our actual ability to model the tidal dynamics. We still need to improve the physics of the tidal models, their overall spatial resolution,

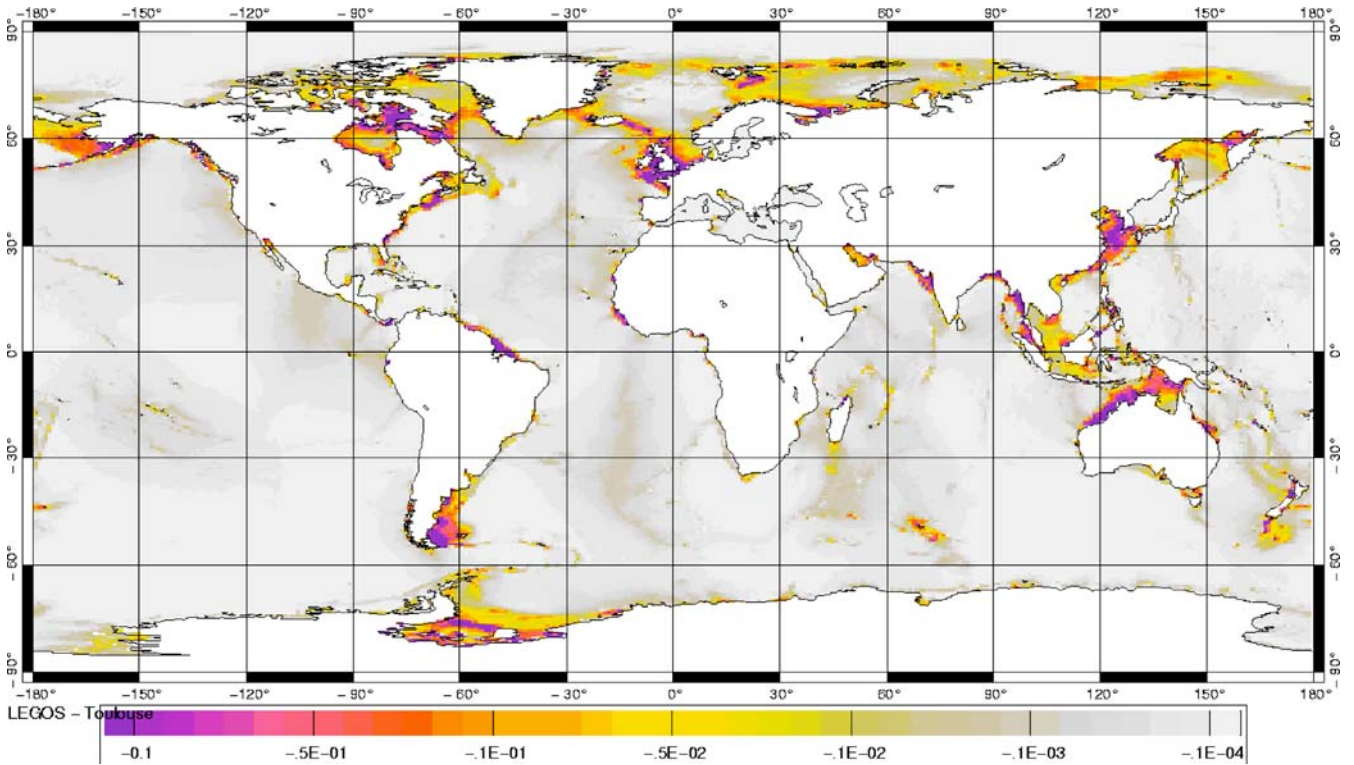


Fig. 8 M_2 bottom friction dissipation (W/m^2)

their energy dissipation through the internal wave generation mechanism and the contribution of LSA effects, which are still mostly computed from pre-existing solutions. Accurate bathymetry is also needed, and present global and regional databases do not fulfil this requirement. New assimilation techniques are to be developed, compatible with time-stepping, non-linear, high-resolution global tidal models. Indeed, the task of continuing to improve global tidal atlases remains.

Acknowledgements Numerical simulations of the hydrodynamic and assimilation codes were performed at the *Institut du Développement et des Ressources en Informatique Scientifique* computational centre (Paris, France). The authors wish to thank all the people who have collaborated in the development of the FES atlases during the past 15 years, including the tidal group of the T/P mission, and the *Centre National d'Etudes Spatiales* for its constant support. They also thank R. Morrow for her encouragement and help in correcting earlier drafts.

Appendix

Block resolution technique

As mentioned earlier, the tidal solutions are computed separately for each of the main oceanic basins. In the FES atlases prior to FES99, the continuity of the solutions along the basins' open limits is obtained by adding some constraints in the assimilation procedures, which are performed on a global basis. This rather simple approach

proved to be not totally satisfying; in particular it was responsible for some local inconsistencies (unbalanced mass or energy budget) and some undesirable side effects on the solution along the shorelines and the open ocean boundaries. To overtake this difficulty, we have developed an additional step in the tidal numerical model which allows us to retrieve the global solutions by merging together the basin-wide simulations. It is based on an approach similar to the block resolution technique, and the so-obtained solution is exactly similar to the one that would be computed on a global FE mesh (as far as the hydrodynamic model is linear).

Let us consider the global problem, obtained by merging the $N-1$ separate basins, with unknowns sorted by basins, except for the unknowns belonging to the open limits which are shared by at least two different basins, which are amalgamated in a N th vector. Under this formalism, the global hydrodynamic problem of $N-1$ basins is equivalent to the following system:

$$\begin{bmatrix} \ddots & 0 & 0 & \vdots \\ 0 & \mathbf{A}_{i,i} & 0 & \mathbf{A}_{i,N} \\ 0 & 0 & \ddots & \vdots \\ \cdots & \mathbf{A}_{N,i} & \cdots & \mathbf{A}_{N,N} \end{bmatrix} \begin{bmatrix} \mathbf{X}_1 \\ \vdots \\ \mathbf{X}_{N-1} \\ \mathbf{X}_N \end{bmatrix} = \begin{bmatrix} \mathbf{Y}_1 \\ \vdots \\ \mathbf{Y}_{N-1} \\ \mathbf{Y}_N \end{bmatrix} \quad (31)$$

where \mathbf{X}_i is the interior unknown vector for oceanic basin i , \mathbf{X}_N the shared open limits unknown vector for basin 1 to $N-1$, \mathbf{Y}_i the tidal forcing for oceanic basin i and \mathbf{Y}_N the tidal forcing along the shared open limits. The zero blocks

in Eq. 30 denote the disconnection between inner nodes belonging to different basins.

The matrix Eq. 30 then yields:

$$\begin{cases} \mathbf{X}_i = \mathbf{A}_{i,i}^{-1}(\mathbf{Y}_i - \mathbf{A}_{i,N}\mathbf{X}_N) \forall i \in \{1, \dots, N-1\} \\ \mathbf{X}_N = \mathbf{A}_{N,N}^{-1}\left(\mathbf{Y}_N - \sum_1^{N-1} \mathbf{A}_{N,i}\mathbf{X}_i\right) \end{cases} \quad (32)$$

The block solution technique consists in eliminating the \mathbf{X}_i in the Eq. 31.

$$\left(\mathbf{A}_{N,N} + \sum_{i=1}^{N-1} \mathbf{A}_{N,i}\mathbf{A}_{i,i}^{-1}\mathbf{A}_{i,N}\right)\mathbf{X}_N = \mathbf{Y}_N - \sum_1^{N-1} \mathbf{A}_{N,i}\mathbf{A}_{i,i}^{-1}\mathbf{Y}_i \quad (33)$$

The difficulty here is that Eq. 32 involves the computation of the inverse of $\mathbf{A}_{i,i}$, which would normally prevent us from using this formulation in a direct method. The solution to this problem would be rather to use an iterative solver instead. However, the inverse matrices are multiplied by matrices such that not all coefficients in the inverse matrices are needed. Actually, the interior unknowns of basin i (i.e. all unknowns except open boundary ones) can be separated into two groups. Group 1 contains unknowns with no direct interactions with the open boundary unknowns. Group 2 contains the ‘‘neighbours’’ of the open boundary unknowns. Sorting the basin interior unknowns into groups 1 and 2 allow us to redefine a simpler problem by rewriting $\mathbf{A}_{N,i}\mathbf{A}_{i,i}^{-1}$, $\mathbf{A}_{i,N}$ as follow:

$$\begin{aligned} \mathbf{A}_{N,i} \times \mathbf{A}_{i,i}^{-1} \times \mathbf{A}_{i,N} &= \underbrace{\begin{bmatrix} 0 & \mathbf{B}_{1,2} \end{bmatrix}}_{\mathbf{A}_{N,i}} \times \underbrace{\begin{bmatrix} \mathbf{C}_{1,1} & \mathbf{C}_{1,2} \\ \mathbf{C}_{2,1} & \mathbf{C}_{2,2} \end{bmatrix}}_{\mathbf{A}_{i,i}^{-1}} \times \underbrace{\begin{bmatrix} 0 \\ \mathbf{D}_{2,1} \end{bmatrix}}_{\mathbf{A}_{i,N}} \\ &= \mathbf{B}_{1,2} \times \mathbf{C}_{2,2} \times \mathbf{D}_{2,1} \end{aligned} \quad (34)$$

The $\mathbf{C}_{2,2}$ term is independently defined for each basin i and has the dimensions of the square of the number of computational nodes which are neighbours of at least one shared open boundary node. It can be efficiently computed using an impulse response technique from the basin, boundary condition constrained models. The basin problem with boundary conditions is given by:

$$\begin{bmatrix} \mathbf{A}_{i,i} & \tilde{\mathbf{A}}_{i,N} \\ 0 & 1 \end{bmatrix} \begin{bmatrix} \mathbf{X}_i^0 \\ \tilde{\mathbf{X}}_N^0 \end{bmatrix} = \begin{bmatrix} \mathbf{Y}_i \\ \tilde{\mathbf{X}}_N \end{bmatrix} \quad (35)$$

where the superscript \sim indicates that the vector/matrix are reduced to their blocks related with the unknowns of basin i . $\tilde{\mathbf{X}}_N^0$ is the restriction of the \mathbf{X}_N^0 vector and represents the open boundary conditions for basin i . In our procedure, this

system is solved for each basin using prior boundary conditions. We can notice that:

$$\begin{aligned} \begin{bmatrix} \mathbf{A}_{i,i} & \tilde{\mathbf{A}}_{i,N} \\ 0 & 1 \end{bmatrix} \times \begin{bmatrix} \mathbf{A}_{i,i}^{-1} & -\mathbf{A}_{i,i}^{-1}\tilde{\mathbf{A}}_{i,N} \\ 0 & 1 \end{bmatrix} \\ = \begin{bmatrix} \mathbf{A}_{i,i}^{-1} & -\mathbf{A}_{i,i}^{-1}\tilde{\mathbf{A}}_{i,N} \\ 0 & 1 \end{bmatrix} \times \begin{bmatrix} \mathbf{A}_{i,i} & \tilde{\mathbf{A}}_{i,N} \\ 0 & 1 \end{bmatrix} = \mathbf{I} \end{aligned} \quad (36)$$

Rewriting Eq. 34 yields:

$$\begin{bmatrix} \mathbf{A}_{i,i}^{-1} & -\mathbf{A}_{i,i}^{-1}\tilde{\mathbf{A}}_{i,N} \\ 0 & 1 \end{bmatrix} \begin{bmatrix} \mathbf{Y}_i \\ \tilde{\mathbf{X}}_N \end{bmatrix} = \begin{bmatrix} \mathbf{X}_i^0 \\ \tilde{\mathbf{X}}_N^0 \end{bmatrix} \quad (37)$$

The most right terms of the right hand-side of Eq. 32 can be computed from the $N-1$ solutions of the basin problems, computed in the preliminary step:

$$\mathbf{A}_{N,i}\mathbf{A}_{i,i}^{-1}\mathbf{Y}_i = \mathbf{A}_{N,i}\mathbf{X}_i^0 - \mathbf{A}_{N,i}\mathbf{A}_{i,i}^{-1}\tilde{\mathbf{A}}_{i,N}\tilde{\mathbf{X}}_N^0 \quad (38)$$

Due to the dynamical disconnection of the interior nodes from different basins, we can infer the following equality:

$$\tilde{\mathbf{A}}_{i,N}\tilde{\mathbf{X}}_N^0 = \mathbf{A}_{i,N}\mathbf{X}_N^0 \quad (39)$$

The solution vector of the shared open boundary nodes is given by:

$$\begin{aligned} \left(\mathbf{A}_{N,N} - \sum_1^{N-1} \mathbf{A}_{N,i}\mathbf{A}_{i,i}^{-1}\mathbf{A}_{i,N}\right)\mathbf{X}_N \\ = \mathbf{Y}_N - \sum_1^{N-1} \mathbf{A}_{N,i}\mathbf{X}_i^0 - \sum_1^{N-1} \mathbf{A}_{N,i}\mathbf{A}_{i,i}^{-1}\mathbf{A}_{i,N}\mathbf{X}_N^0 \end{aligned} \quad (40)$$

Due to the integral formulation of the wave equation, the $\mathbf{A}_{\rightarrow,N}$ blocks of the dynamic equations of the shared open boundary nodes can be easily obtained by adding the partial dynamic equations formed for the basin-wide problems. After Eq. 39 has been solved, the global solution is obtained by applying the following formula to each basin:

$$\mathbf{X}_i = \mathbf{A}_{i,i}^{-1}(\mathbf{Y}_i - \mathbf{A}_{i,N}\mathbf{X}_N) = \mathbf{X}_i^0 + \mathbf{A}_{i,i}^{-1}\mathbf{A}_{i,N}(\mathbf{X}_N^0 - \mathbf{X}_N) \quad (41)$$

Again $\mathbf{A}_{i,i}^{-1}\mathbf{A}_{i,N}$ involves only a limited number of coefficients of the inverse matrix, i.e. the coefficients related to open boundary nodes. Those necessary coefficients can be efficiently computed using an impulse response technique from the basin, boundary condition constrained models. In practice, the tidal problem is solved

for each basin, and impulse response is simultaneously computed for the shared open boundary nodes and their immediate neighbours. Then the block resolution is carried out. The data assimilation uses the same approach for the backward and forward systems, except that no specific nor additional impulse response computations are needed (the impulse responses of the adjoint system are the complex conjugate of the impulse responses of the direct system). Note that in a linear problem, the prior boundary conditions are of no influence at all, and could be set to zero. In practice, specifying realistic boundary conditions is necessary for the (non-linear) dominant wave case and for computing realistic friction coefficients. This step also allows a quality control of the basin's computation for the other (linearized) waves before passing to the computation of the global solution.

References

- Accad Y, Pekeris CL (1978) Solution of the tidal equations for the M_2 and S_2 tides in the world oceans from a knowledge of the tidal potential alone. *Philos Trans R Soc Lond Ser A Math Phys Sci* 290:235–266
- Andersen OB, Egbert GD, Erofeeva SY, Ray RD (2006) Mapping nonlinear shallow-water tides: a look at the past and future (in press). DOI [10.007/s10236-006-0060-7](https://doi.org/10.007/s10236-006-0060-7)
- Arbic BK (2005) Atmospheric forcing of the oceanic semidiurnal tide. *Geophys Res Lett* 32:L02610, DOI [10.1029/2004GL021668](https://doi.org/10.1029/2004GL021668)
- Bell TH (1975) Topographically generated internal waves in the open ocean. *J Geophys Res* 80:320–327
- Bennett AF (1990) Inverse methods for assessing ship-of-opportunity networks and estimating circulation and winds from tropical expendable bathythermograph data. *J Geophys Res* 95 (C9):16111–16148
- Bennett AF, McIntosh PC (1982) Open ocean modelling as an inverse problem. *J Phys Oceanogr* 12:1004–1018
- Carrère L (2003) Etude et modélisation de la réponse haute fréquence de l'Océan global aux forçages météorologiques. Ph.D. thesis, Université III Paul Sabatier
- Carrère L, Lyard F (2003) Modeling the barotropic response of the global ocean to atmospheric wind and pressure forcing—comparisons with observations. *Geophys Res Lett* 30(6):1275, DOI [10.1029/2002GL016473](https://doi.org/10.1029/2002GL016473)
- Carrère L, Le Provost C, Lyard F (2004) On the statistical stability of the M_2 barotropic and baroclinic tidal characteristics from along-track TOPEX/Poseidon satellite altimetry analysis. *J Geophys Res* 109:C03033
- Cartwright DE, Ray RD (1991) Energetics of global ocean tides from Geosat altimetry. *J Geophys Res* 96(C9):16897–16912
- Cartwright DE, Spencer R (1988) The tides of the Atlantic Ocean. *Philos Trans R Soc Lond A* 324:513–563
- Chabert d'Hières G, Le Provost C (1978) Atlas des composantes harmoniques de la marée dans la Manche. *Ann Hydrogr* 46:5–35
- Egbert G, Ray RD (2000) Significant dissipation of tidal energy in the deep ocean inferred from satellite altimeter data. *Nature* 405:775–778
- Egbert GD, Ray RD (2001) Estimates of M_2 tidal energy dissipation from Topex/Poseidon altimeter data. *J Geophys Res* 106:22475–22502
- Egbert GD, Ray RD (2003) Deviation of long period tides from equilibrium: kinematics and geostrophy. *J Phys Oceanogr* 33:822–839
- Egbert GD, Bennett AF, Foreman GG (1994) TOPEX/POSEIDON tides estimated using a global inverse model. *J Geophys Res* 99:24,821–24,852
- Egbert GD, Ray RD, Bills BG (2004) Numerical modeling of the global semidiurnal tide in the present day and in the last glacial maximum. *J Geophys Res* 109:C03003, DOI [10.1029/2003JC001973](https://doi.org/10.1029/2003JC001973)
- Farrell WE (1972) Deformation of the earth by surface loads. *Rev Geophys Space Phys* 10:761–797
- Francis O, Mazzega P (1990) Global charts of ocean tide loading effects. *J Geophys Res* 95(C7):11411–11424
- Genco ML, Lyard F, Le Provost C (1994) The Oceanic tides in the South Atlantic Ocean. *Ann Geophys* 12:868–886
- Greenberg D, Dupont F, Lyard F, Lynch DR, Werner FE (2006) Resolution issues in numerical models of Oceanic and coastal circulation. *Cont Shelf Res* (in press)
- Groves GW, Reynolds RW (1975) An orthogonalized convolution method of tide prediction. *J Geophys Res* 80:4131–4138
- Jayne SR, St. Laurent LC (2001) Parameterizing tidal dissipation over rough topography. *Geophys Res Lett* 28:811–814
- Le Provost C, Fornerino M (1985) Tidal spectroscopy of the English Channel with a numerical model. *J Phys Oceanogr* 15(8):1009–1031
- Le Provost C, Lyard F (1998) Energetics of the M_2 barotropic ocean tides: an estimate of bottom friction dissipation from a hydrodynamic model. *Prog Oceanogr* 40:37–52 (special issue on tidal science in honour of David E. Cartwright)
- Le Provost C, Vincent P (1986) Some tests of precision for a finite element model of ocean tides. *J Comput Phys* 65:273–291
- Le Provost C, Poncet A, Rougier G (1981) Numerical modelling of the harmonic constituents of the tides—application to the English Channel. *J Phys Oceanogr* 11(8):1123–1138
- Le Provost C, Lyard F, Molines JM (1991) Improving Ocean tides predictions by using additional semidiurnal constituents from spline approximation in the frequency domain. *Geophys Res Lett* 18(5):845–848
- Le Provost C, Bennett AF, Cartwright DE (1995) Ocean tides for and from TOPEX/POSEIDON. *Science* 267:639–642
- Le Provost C, Lyard F, Genco ML, Rabilloud F (1998) A hydrodynamic ocean tide model improved by assimilation of a satellite altimeter-derived data set. *J Geophys Res* 103 (C3):5513–5529
- Lefevre F (2004) Modélisation des marées océaniques à l'échelle globale : assimilation de données in situ et altimétriques. Ph.D. thesis, Université III Paul Sabatier
- Lefevre F, Lyard F, Le Provost C, Schrama EJO (2002) FES99: a global tide finite element solution assimilating tide gauge and altimetric information. *Atmos Ocean Tech* 19:1345–1356
- Letellier T (2004) Etude des ondes de marée sur les plateaux continentaux. Ph.D. thesis, Université III Paul Sabatier
- Lewellyn Smith SG, Young WR (2002) Conversion of the barotropic tide. *J Phys Oceanogr* 32:1554–1566
- Lyard F (1999) Data assimilation in a wave equation: a variational representer approach for the Grenoble tidal model. *J Comput Phys* 149:1–31
- Morozov E (1995) Semidiurnal internal wave global field. *Deep-Sea Res Part 1 Oceanogr Res Pap* 42:135–148
- Munk WH, Cartwright DE (1966) Tidal spectroscopy and prediction. *Philos Trans R Soc Lond A* 259:533–581
- Munk W, Wunsch C (1998) Abyssal recipes II: energetics of tidal and wind mixing. *Deep-Sea Res Part 1 Oceanogr Res Pap* 45:1977–2010
- Ponchaut F, Lyard F, Le Provost C (2001) An analysis of the tidal signal in the WOCE Sea level dataset. *J Atmos Ocean Technol* 18:77–91
- Ray RD (1999) A global ocean tide model from TOPEX/POSEIDON altimetry: GOT99. NASA technical memorandum 209478. Goddard space flight centre, Greenbelt
- Ray RD, Egbert GD (2004) The global S_1 tide. *J Phys Oceanogr* 34:1922–1935
- Ray RD, Mitchum GT (1996) Surface manifestation of internal tides generated near Hawaii. *Geophys Res Lett* 23(16):2101–2104
- Ray RD, Ponte RM (2003) Barometric tides from ECMWF operational analyses. *Ann Geophys* 21:1897–1910
- Schrama E, Ray RD (1994) A preliminary tidal analysis of TOPEX/POSEIDON altimetry. *J Geophys Res* 99:24799–24808

- Schwiderski EW (1980) Ocean tides, II, a hydrodynamic interpolation model. *Mar Geod* 3:219–255
- Shum CK, Woodworth PL, Andersen OB, Egbert G, Francis O, King C, Klosko S, Le Provost C, Li X, Molines JM, Parke M, Ray R, Schlax M, Stammer D, Temey C, Vincent P, Wunsch C (1997) Accuracy assessment of recent ocean tide models. *J Geophys Res* 102(C11):25173–25194
- Simmons H, St Laurent L, Jayne S, Weaver A (2004a) Tidally driven mixing in a numerical model of the ocean general circulation. *Ocean Model* 6:245–263
- Simmons H, Hallberg R, Arbic B (2004b) Internal wave generation in a global baroclinic tide model. *Deep-Sea Res Part 2 Top Stud Oceanogr* 51:3043–3068, DOI [10.1016/j.dsr2.2004.09.015](https://doi.org/10.1016/j.dsr2.2004.09.015)